Available online at www.sciencedirect.com
SCIENCE DIRECT®
ELSEVIER
International Journal of Solids and Structures 43 (2006) 4546–4577
INTERNATIONAL JOURNAL OF SOLIDS and STRUCTURES
www.elsevier.com/locate/ijsolstr

Numerical investigation of grain boundary effects on elevated-temperature deformation and fracture

Yan-Qing Wu [a,*], Hui-Ji Shi [a], Ke-Shi Zhang [b], Hsien-Yang Yeh [c]

[a] *State Key Laboratory of Failure Mechanics, Department of Engineering Mechanics, Tsinghua University, Beijing 100084, PR China*
[b] *Department of Engineering Mechanics, Northwestern Polytechnical University, Xi'an 710072, PR China*
[c] *Department of Mechanical and Aerospace Engineering, 1250 Bellflower Boulevard, California State University, Long Beach, CA 90840-8305, USA*

Received 15 March 2005; received in revised form 17 June 2005
Available online 22 August 2005

Abstract

A three-dimensional (3D) polycrystal intergranular model that accounts for grain boundary deformation and intergranular weakening at elevated temperatures is presented. The effects of grain boundaries on the accumulated slip deformation of grain interiors and lattice rotation have been investigated through a comparison between results from a model including grain boundary region (GBM) and a model representing only the grain interiors not the grain boundary region directly (NGBM). It is found that the presence of grain boundaries seems to suppress the grain interior slip deformation, and this suppressive role is reduced with increased relative thickness of the grain boundaries. In addition, grain boundaries promote the lattice rotation of individual grains in shear bands but suppress that of individual grains within non-shear bands. Mutual rotation of grains in both shear and non-shear bands is caused by the introduction of grain boundary regions. Rate-dependence of high-temperature plasticity could be more accurately captured by the GBM than by the NGBM. By considering creep damage of grain boundary, when the damage variable reaches a critical value, the corresponding grain boundary element is eliminated to describe dynamic intergranular fracture processes. The volume-averaged stress–strain curve by a model considering grain boundary damage (DGBM) showed better agreement with experimental results than that by a model not considering grain boundary damage (GBM).

Keywords: Grain boundary effects; Polycrystal deformation; Lattice rotation; Intergranular fracture; Shear band; Elevated temperature

* Corresponding author. Tel.: +86 10 6277 1817; fax: +86 10 6278 1824.
E-mail address: wuyqing@mail.tsinghua.edu.cn (Y.-Q. Wu).

0020-7683/$ - see front matter © 2005 Elsevier Ltd. All rights reserved.
doi:10.1016/j.ijsolstr.2005.06.075

1. Introduction

Advances in the field of the plasticity of single crystals have made it possible for room-temperature plastic deformation of polycrystals to be analyzed numerically in great detail (Nakamachi et al., 2000; Meissonnier et al., 2001). When the temperature increases, more intergranular phenomena are involved leading to very complex micro- and mesoscopic phenomena. Grain size control has frequently been studied for high-temperature behaviors of polycrystals (Hasegawa et al., 1998; Lee et al., 2002). Bower and Wininger (2004) developed a detailed microstructural model including all the processes that may play a role in superplastic flow, and may capture some of the characteristics in high-temperature deformation as well.

For most widely used materials without any special grain size treatment, Hanson and Wheeler (1931) noted that some of the changes in grain boundary structure were characterized by widely spaced marks at elevated temperatures. Langdon (1993) presented a brief overview of the role of grain boundaries in flow and fracture at high temperatures and concluded that it is appropriate to define four grain size ranges with reasonably similar flow and fracture characteristics. The contribution of grain boundary to high-temperature deformation has also been reviewed by Gifkins (1994). The presence of grain boundaries is important for the deformation behavior and the mechanical properties of crystals.

Bicrystal experimentation appears to be one of the most effective methods to investigate the grain boundary behavior quantitatively (Yoshida et al., 2004). However, for polycrystals under elevated temperatures, the corresponding experimental verification does not provide highly quantitative insights into the micromechanical processes of crystal plasticity. Numerical simulation seems to be a good way to study the effects of the grain boundaries on individual grain behavior. Mecking (1981) suggested the conceptual linkage of various regions within a polycrystalline aggregate. Therefore, for numerical calculations, the polycrystalline aggregate has been used as a composite comprised of a grain interior with flow stress σ_{fG} and the grain boundary regions with flow stress σ_{fGB} (Meyers et al., 2002).

Thickness t was assigned to the grain boundaries and assumed to vary with grain size as follows:

$$t = k_{\mathrm{MA}} D^{1/2} \tag{1}$$

where k_{MA} is the material's constant and D is the grain size.

Most experimental observations have shown that the presence of a small amount of liquid at interfaces or grain boundaries will assist strain accommodation (Takayama et al., 1999; Koike et al., 1995). Cao et al. (1996) reported that the viscous flow of liquid-like substances originally exists at the grain boundaries and suggested the mechanism of grain boundary sliding could also be the viscous flow of the grain boundary materials. The limited information available suggests that the grain boundary viscous flow is not as strongly dependent on the lattice misorientation as grain interiors are. Shen et al. (2000) analyzed the high-temperature deformation of a polycrystalline structure based on a continuum framework, in which the grain boundary region and grain interior region were both taken as rate-independent plasticity.

In the present model, these ideas are extended in a new model based on high-temperature deformation mechanisms of an Al–Cu–Mg polycrystals. Instead of the topological complexity of a real polycrystal aggregate, a regular grain shape was used, allowing the study of significant influences of grain boundaries on deformation and fracture at elevated temperatures. At present, the mechanism behind the production of the dislocations at grain boundaries is not very clear. It may be appropriate to use Chaboche constitutive equations to describe grain boundary deformation that include creep and relaxation phenomena at the same time. The grains are deformed plastically by thermally activated dislocation motion, which we modeled using a conventional rate-dependent crystal plasticity law.

Zavattieri and Espinosa (2001) embedded the cohesive interface elements along grain boundaries to simulate intergranular fracture through microcrack initiation, propagation and coalescence for brittle materials such as ceramics. Their model provides a powerful tool for predicting the structural response of naturally brittle materials (Zavattieri et al., 2001). In addition, Tvergaard (2004) extended the interface

elements to cover non-symmetric mixed mode loading conditions for crack growth along an interface between dissimilar elastic–plastic solids. This kind of interface description takes into account the effects of stress triaxiality on damage evolution. Even though the use of cohesive laws based on displacement jumps for interface elements seems to be a promising approach, it is more suitable for brittle fracture evolution which depends strongly on local cracks opening.

At high temperatures, grain boundaries are a potential source of weakness because they provide both nucleation sites for cavities and paths for the interlinkage of cavities to form intergranular cracks (Langdon, 1993). As the temperature is increased above approximately $0.4T_m$ (T_m is the absolute melting temperature), the fracture mode is generally intergranular. For the present Al–Cu–Mg alloy, representative scanning electronic microscopy (SEM) micrographs for the specimen tensioned to fracture at room and high temperatures are shown in Fig. 1, in which the fractographs are compared at room temperature and 753 K. It is clear that intergranular ductile fracture dominates the fracture process at temperature of higher than $0.4T_m$. Furthermore, Fig. 2 shows the intergranular morphologies observed by transmission electronic microscopy (TEM), in which both (b) and (c) exhibit obvious intergranular caviatation and fracture characteristics as a result of rise in temperature.

Based on SEM and TEM analysis, it is effective to describe rate-dependent void damage of grain boundaries under the assumption of no transgranular fracture. Intergranular cavitation and fracture in general are the consequence of creep damage (Hermann, 1987), so it may be appropriate to use Rabotnov creep damage law and isotropic damage variable to represent the intergranular failure. From physical view,

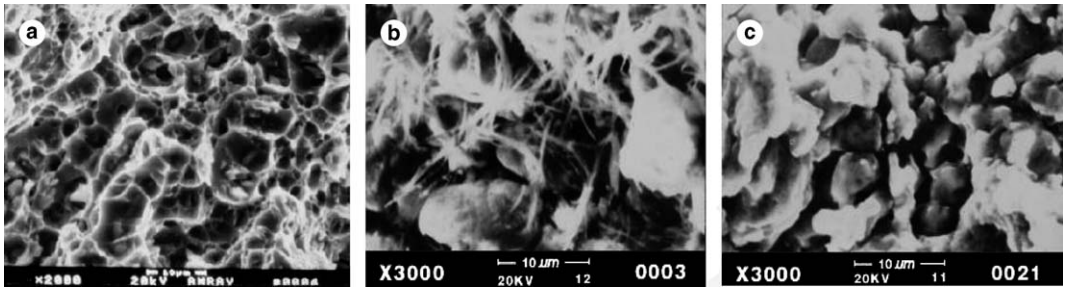

Fig. 1. Fracture surface of Al–Cu–Mg alloy through SEM observations representing: (a) dimple rupture mode of samples tensile tested at room temperature; (b) intergranular fracture mode of samples tensile tested at 10^{-4} s^{-1} and 753 K; (c) intergranular fracture mode of sample tensile tested at 10^{-1} s^{-1} and 753 K.

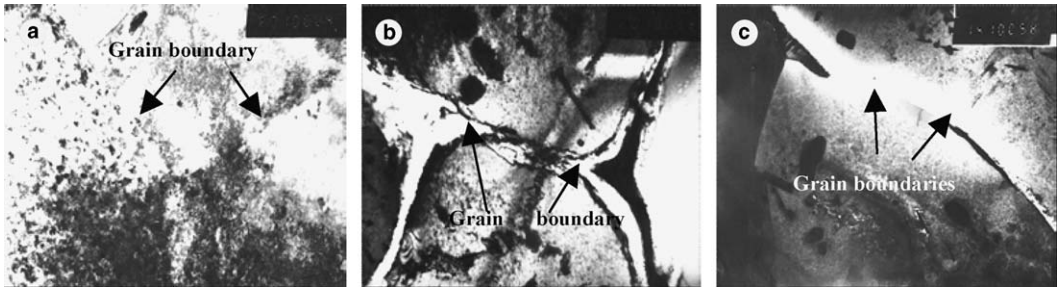

Fig. 2. TEM analysis of grain boundary morphology for the deformed Al–Cu–Mg alloy sample tensioned to fracture (a) at room temperature showing almost no participation of grain boundaries during deformation (b) at 10^{-4} s^{-1} and 713 K as well as (c) at 10^{-4} s^{-1} and 753 K indicating the participation of grain boundary in deformation which are related to dependence of intergranular fracture upon temperature.

isotropic damage variable applied to grain boundaries is considered to be the homogeneous distributed microvoids along grain boundary. In a metallographic assessment, the isotropic damaged variable is introduced into the grain boundary would correspond to the area of transverse grain boundaries occupied by cavities. Based on this, the present paper evaluates the effects of intergranular phenomena with concurrence of intragranular heterogeneities of the stress and strain. To provide a continuous representation of time-dependent intergranular fracture processes, an element would be eliminated when the damage variable of the element reaches a critical value because it has lost its load-carrying ability. A user-defined material subroutine (UMAT) is implemented in the finite element code ABAQUS incorporating both grain boundary constitutive model and grain interior crystal model. 'Model Change' function in ABAQUS is used to remove the failure elements.

2. Constitutive equations

2.1. Rate-dependent crystal model for grain interior

Because the exact relationship between flow stress and dislocation interaction has not yet been quantitatively obtained, simulation of polycrystal deformation is generally based on single crystal slip plastic deformation theory. According to Hutchinson (1976), rate-dependent flow rule for describing a slip system is

$$\dot{\gamma}^{(\alpha)} = \dot{\gamma}_0 \mathrm{sgn}(\tau^{(\alpha)}) \left| \frac{\tau^{(\alpha)}}{g^{(\alpha)}} \right|^{1/m_{\mathrm{GI}}} \tag{1}$$

m_{GI} characterizes the rate sensitivity of grain interior shearing slip. $\dot{\gamma}_0$ is the reference shear rate. $\tau^{(\alpha)}$ is the resolved shear stress on the slip system α, which is given by the Schmid law

$$\tau^{(\alpha)} = \frac{1}{2}(\mathbf{m}^{(\alpha)} \otimes \mathbf{n}^{(\alpha)} + n^{(\alpha)} \otimes \mathbf{m}^{(\alpha)}) : \boldsymbol{\sigma} \tag{2}$$

where $\boldsymbol{\sigma}$ is the Cauchy stress with respect to current configuration. $\mathbf{m}^{(\alpha)}$ and $\mathbf{n}^{(\alpha)}$ denote the unit vector along the slip direction the normal direction of the α-slip system at current time respectively. The evolution of the function $g^{(\alpha)}(\gamma)$ specifies the material strain hardening

$$\dot{g}^{(\alpha)} = \sum_{\beta=1}^{n} h_{\alpha\beta} |\dot{\gamma}^{(\beta)}| \tag{3}$$

Hutchinson (1976) suggested that the slip-plane hardening law could be given as

$$h_{\alpha\beta}(\gamma) = h(\gamma)[q + (1-q)\delta_{\alpha\beta}] \tag{4}$$

$$h(\gamma) = h_0 \mathrm{sech}^2 \left\{ \frac{h_0 \gamma}{\tau_s - \tau_0} \right\} \tag{5}$$

$$\gamma = \int_0^t \sum_{\alpha=1}^{n} |\dot{\gamma}^{(\alpha)}| \mathrm{d}t \tag{6}$$

where q represents the ratio of latent hardening to self hardening on non-coplanar slip systems, h_0 is material parameter. τ_0 is the critical shear stress and τ_s is the saturation shear stress for all slip systems. When $\alpha = \beta$, $\delta_{\alpha\beta} = 1.0$, when $\alpha \neq \beta$, $\delta_{\alpha\beta} = 0.0$. For the aluminum alloy with FCC crystal structure, there are 12 slip systems.

Crystal elasticity is presumed to be unaffected by slip and the elastic strain is related to the stress through

$$\dot{\boldsymbol{\sigma}} = \mathbf{C} : \mathbf{D}^{\mathrm{e}} \tag{7}$$

$\dot{\boldsymbol{\sigma}}$ and $\mathbf{D}^{e}$ are the material time derivative of Cauchy stress and elastic stretching rate tensor respectively. $\mathbf{C}$ is the fourth order tensor of material elastic properties. The detailed algorithm is presented in Zhang et al. (2005).

For the studied Al–Cu–Mg alloy, the elastic properties for crystal model are obtained by introducing aluminum single lattice type. On the basis of aluminum single crystal elastic properties at high temperature, elastic properties of Al–Cu–Mg single crystal are calibrated by performing the uniaxial tensile calculation on a cubic polycrystal model including $10 \times 10 \times 10$ elements and each element represents a single crystal as shown in Fig. 3(a).

The elastic constitutive matrix with cubic symmetry for FCC lattice type is written as

$$[C^{e}] = \begin{bmatrix} C_{1111} & C_{1122} & C_{1122} & 0 & 0 & 0 \\ C_{1122} & C_{1111} & C_{1122} & 0 & 0 & 0 \\ C_{1122} & C_{1122} & C_{1111} & 0 & 0 & 0 \\ 0 & 0 & 0 & C_{2323} & 0 & 0 \\ 0 & 0 & 0 & 0 & C_{2323} & 0 \\ 0 & 0 & 0 & 0 & 0 & C_{2323} \end{bmatrix} \tag{8}$$

where

$$C_{1111} = E_{[100]}(1 - v^2)/(1 - 3v^2 - 2v^3) \tag{9}$$

$$C_{1122} = E_{[100]}(v + v^2)/(1 - 3v^2 - 2v^3) \tag{10}$$

$$C_{2323} = G \tag{11}$$

Thus, the elastic parameters are validated through fitting the test data at 753 K, which is shown in Fig. 3(b).

$$E_{[100]} = 10.724\ \text{GPa}, \quad v = 0.323, \quad G = 4.716\ \text{GPa}$$

$$v12 = v21 = v23 = v32 = v13 = v31 = v = 0.323$$

Besides the elastic constants, the slip system parameters including initial critical shear stress τ_0 which is assumed to be the same for all the slip systems. The fact that slip deformation along slip systems shows strain rate sensitivity suggests choosing $1 > m_{GI} > 0.3$. Thus, the saturation shear stress τ_s, the initial hardening parameters h_0 and the ratio of latent hardening to self hardening q are determined by uniaxial tensile tests combined with the polycrystal aggregate numerical experiments.

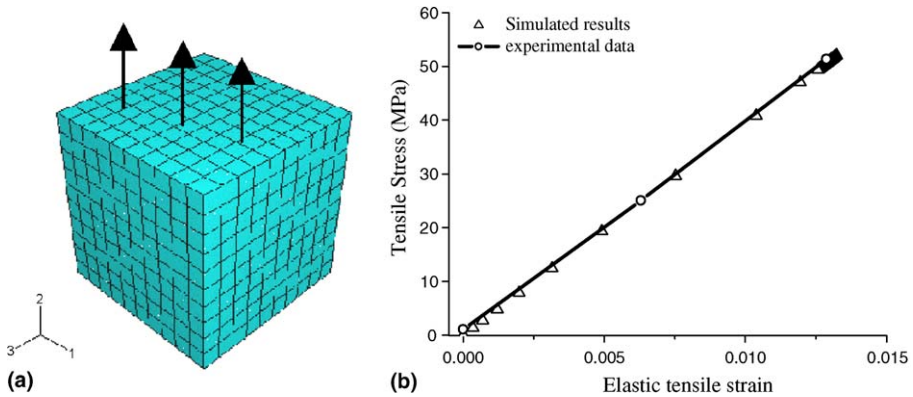

Fig. 3. Calibration curve for Al–Cu–Mg polycrystal elastic uniaxial tension: (a) polycrystal aggregate model subjected to periodic boundary conditions; (b) comparison of computed mean stress–volumetric strain response with experimental data.

In order to eliminate the anisotropic responses of overall polycrystal due to the single crystal slip mechanisms, numerical experiments with alternate 1, 2, and 3 tensile directions are implemented. The polycrystal aggregate with $10 \times 10 \times 10$ cubic elements is also used. Then the overall behaviors (i.e. tensile stress vs. strain) of the aggregate are compared, by averaging all grains in the polycrystal aggregate. The volume-averaged tensile stress is

$$\bar{\sigma}_i = \frac{1}{V}\int_V \sigma_{ii}\,\mathrm{d}V \tag{12}$$

where 'i' in $\bar{\sigma}_i$ and σ_{ii} denoted the tensile direction in terms of the numerical experiments. By modeling an aggregate consisting of $10 \times 10 \times 10$ cubic elements with alternative x-, y-, z-tensile directions to fit the parameters, the slip system parameters are obtained as shown in Table 1. Simulations using the crystal parameters show good agreements with the experimental results (shown in Fig. 4). It is also noticed that simulation using crystal model could not accurately describe the uniaxial damage and fracture stage.

2.2. Chaboche viscoplastic model for grain boundary

Isotropic Chaboche viscoplastic equations with kinematic hardening are used to simulate the viscous flow of grain boundary zones. Back stress is to express interaction of intergranular stresses caused by plastic strains and interactions between dislocations and precipitates. The viscoplastic stretching rate is given as (Lemaitre and Chaboche, 1990)

$$\mathbf{D}^{\mathrm{vp}} = \frac{3}{2}\dot{p}\frac{(\boldsymbol{\sigma}-\mathbf{X})}{J_2(\boldsymbol{\sigma}-\mathbf{X})} \tag{13}$$

$$\dot{p} = \left\langle \frac{J_2(\boldsymbol{\sigma}-\mathbf{X}) - k_0 - R}{K} \right\rangle^{1/m_{\mathrm{GB}}} \tag{14}$$

Table 1
Slip system parameters of single crystal for the Al–Cu–Mg alloy at 480 °C

τ_0 (Mpa)	τ_s (Mpa)	h_0	q	$\dot{\gamma}_0(\mathrm{s}^{-1})$	m_{GI}
16.5	17.5	15.0	0.1	0. 1	0.362

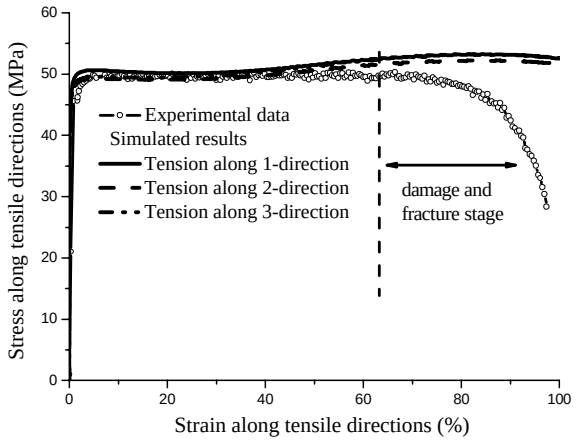

Fig. 4. Comparisons between simulated results by numerical experiments with alternative tensile directions and experimental results.

m_{GB} characterizes the rate-sensitivity of grain boundary behavior. k_0 corresponds to yield stress at zero plastic strain. J_2 is defined as

$$J_2(\boldsymbol{\sigma}-\mathbf{X})=\sqrt{\frac{3}{2}(\boldsymbol{\sigma}'-\mathbf{X}'):(\boldsymbol{\sigma}'-\mathbf{X}')} \tag{15}$$

The MacCauley bracket in Eq. (14) is defined as

$$\langle y\rangle = y \quad \text{if } y>0 \quad \text{and} \quad \langle y\rangle = 0 \quad \text{if } y<0 \tag{16}$$

In finite deformation, the material objective rate of back stress $\mathbf{X}$ is

$$\overset{\nabla}{\mathbf{X}} = c\dot{p}\cdot\left[a(p)\frac{\boldsymbol{\sigma}'-\mathbf{X}'}{J_2(\boldsymbol{\sigma}-\mathbf{X})}-\Phi(p)\mathbf{X}\right]-d\frac{\mathbf{X}}{J_2(\mathbf{X})}\left[\frac{J_2(\mathbf{X})}{a(p)}\right]^r \tag{17}$$

$\Phi(p)$ represents the relaxation function and R describes the isotropic hardening property. p is the total plastic strain given by

$$p=\int_0^t\left\langle\frac{J_2(\boldsymbol{\sigma}-\mathbf{X})-k_0-R}{K}\right\rangle^{1/m_{GB}}\mathrm{d}t \tag{18}$$

Elastic strain is comparatively small compared to plastic strain. Since it is assumed that the current and reference configurations are indistinguishable, we replace the Kirchhoff stress $\boldsymbol{\tau}$ with the Cauchy stress $\boldsymbol{\sigma}$. For finite deformation, Jaumann rate of Cauchy stress $\overset{\nabla}{\boldsymbol{\sigma}}$ at current configuration

$$\overset{\nabla}{\boldsymbol{\sigma}} = \dot{\boldsymbol{\sigma}}-\mathbf{W}\cdot\boldsymbol{\sigma}+\boldsymbol{\sigma}\cdot\mathbf{W} \tag{19}$$

The material spin $\mathbf{W}=(\mathbf{L}-\mathbf{L}^{\mathrm{T}})/2$ and the velocity gradient is given as $\mathbf{L}=\dot{\mathbf{F}}\cdot\mathbf{F}^{-1}$. The Jaumann rate of Cauchy stress is related to elastic stretching rate $\mathbf{D}^{\mathrm{e}}$

$$\overset{\nabla}{\boldsymbol{\sigma}} = 2G\,\mathbf{D}^{\mathrm{e}}+\lambda\mathrm{tr}(\mathbf{D}^{\mathrm{e}})\mathbf{I} \tag{20}$$

$$\mathbf{D}^{\mathrm{e}}=\mathbf{D}-\mathbf{D}^{\mathrm{vp}} \tag{21}$$

To determine the parameters for grain boundary constitutive model, grain boundary is assumed to show the same flow properties as the global specimen. Under this assumption, the details of Chaboche model parameters determination could refer to the literature (Wu, 2003), and so the material parameters used herein are presented in Table 2.

2.3. Grain boundary damage

Various models have been developed to describe grain boundary void nucleation, e.g. void nucleation through continuous shrink and coalescence of grain boundary cavities (Kim et al., 1992), cavities coalescence resulting from stress concentration owning to strain mismatch and grain boundary sliding (Raj and Ashby, 1975), breaking of atomic bonds due to stress concentration by dislocation trapped at grain boundaries (Fleck et al., 1975). In fact, it is difficult to identify the one that grows from zero size and that

Table 2
Model parameters for grain boundary (those without parentheses are dimensionless)

E (Mpa)	v	k (MPa)	m_{GB}	K (MPa)	Q (MPa)	b	c
15598	0.33	35.50	0.464	30.8682	3.0	45.0	97.879
ω_1	d (MPa)	r	a_0 (MPa)	a_1 (MPa)	ϕ_∞	ω_0	
1.0e−9	0.001	1.0	4.33	5.79	1.0	1.0e−9	

from one having existed on interface or grain boundaries among the observed voids. Thus, to simulate the contribution of grain boundary cavitation damage to overall deformation and intergranular fracture process, continuum damage theory is specified for describing damage of grain boundaries based on Rabotnov creep damage law (1969). So the isotropic damaged variable Φ follows:

$$\dot{\Phi} = \left(\frac{\sigma_{eq}}{B}\right)^{n} (l - \Phi)^{-l} \tag{22}$$

B, n and l are material parameters, and σ_{eq} is the equivalent stress. Φ is usually explained as the loss of loading ability due to material property deterioration, and $(1 - \Phi)^{-l}$ is derived from the concept of effective stress describing deformation approaching the final fracture stage.

Generally, the isotropic damage variable can be written as

$$\Phi = \frac{A - A^*}{A} = 1 - \frac{A^*}{A} \tag{23}$$

where A is the original undamaged area and A^* is the effective damaged area. The relationship between effective Cauchy stress $\boldsymbol{\sigma}_{eff}$ and nominal stress $\boldsymbol{\sigma}$ is defined as

$$\boldsymbol{\sigma}_{eff} = \frac{1}{1 - \Phi}\boldsymbol{\sigma} \tag{24}$$

According to the extended Hook law,

$$\boldsymbol{\sigma}_{eff} = \mathbf{C} : \boldsymbol{\varepsilon}^{el} \tag{25}$$

$\mathbf{C}$ is the isotropic elastic constitutive tensor and ε^{el} is the elastic strain tensor, $\boldsymbol{\sigma}_{eff}$ is the effective Cauchy stress tensor

$$\boldsymbol{\sigma} = (1 - \Phi)\boldsymbol{\sigma}_{eff} = (1 - \Phi)\mathbf{C} : \boldsymbol{\varepsilon}^{el} \tag{26}$$

Due to the introduction of damage variable Φ, the elastic response is governed by the following equation

$$\overset{\nabla}{\boldsymbol{\sigma}} = 2G\mathbf{D}^{e} + \lambda \operatorname{tr}(\mathbf{D}^{e})\mathbf{I} - \frac{\dot{\Phi}}{1 - \Phi}\boldsymbol{\sigma} \tag{27}$$

3. Details of the finite element method (FEM) analysis

3.1. Polycrystal aggregate model

Before implementing the polycrystal simulations, macroscopic uniaxial tension simulations are performed first using the Chaboche viscoplastic model to derive the loading conditions, which are schematically described in Fig. 5. Two polycrystal aggregates are constructed: the model consisting of grain boundary regions (GBM) and not consisting of grain boundary regions (NGBM), as shown in Fig. 5(b) and (c). l_x, l_y, and l_z refer to the size of the representative volume element (RVE) along three coordinate directions. As described before, the grain boundary and the grain interior behavior are modeled by different constitutive models.

The mixed displacement and pressure loading conditions applied to the polycrystal aggregate model are described as follows:

$$u_x(0, y, z) = 0, \quad u_y(x, 0, z) = 0, \quad u_z(x, y, 0) = 0 \tag{28a}$$

$$u_x(l_x, y, z) = u_x(l_x, 0, 0), \quad u_z(x, y, l_z) = u_z(0, 0, l_z) \tag{28b}$$

$$u_y(x, l_y, z, t) = U_y(t) \tag{28c}$$

$$P^{x=l_x}_{surf} = \bar{\sigma}_{ij}(t) n_j^{x=l_x}, \quad P^{z=l_z}_{surf} = \bar{\sigma}_{ij}(t) n_j^{z=l_z} \tag{28d}$$

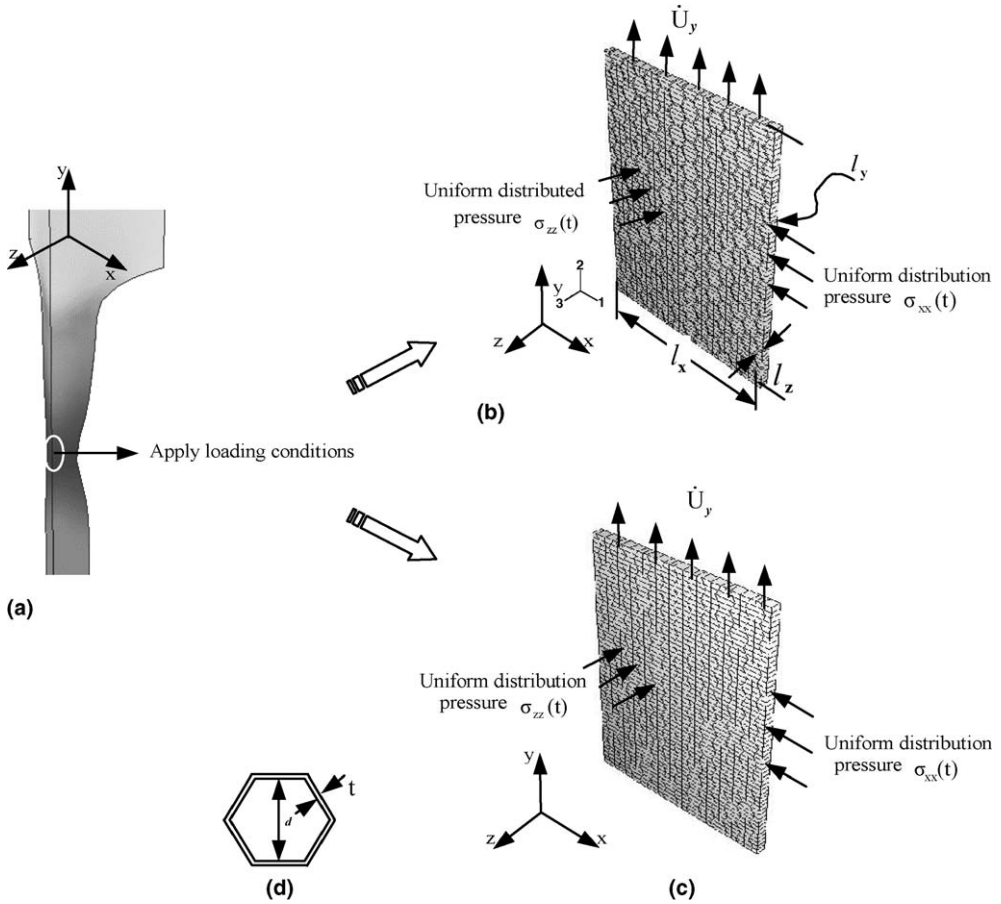

Fig. 5. Schematic graphs showing the detailed simulation techniques: (a) macroscopic deformed specimen; (b) boundary conditions for GBM (model consisting of grain boundary regions); (c) boundary conditions for NGBM (model not consisting of grain boundary regions); (d) grain diameter and grain boundary thickness.

where $\bar{\sigma}_{ij}(t)$ denotes the stress tensor components averaged over the volume of the target element in the necked region and the summation convention for repeated indices is applied. Eq. (28b) gives the constraint conditions that all points on surfaces $x = l_x$ and $z = l_z$ should satisfy, ensuring the points lie in the same plane all through so that $n_j^{x=l_x}$ and $n_j^{z=l_z}$ do not change with time. Eq. (28d) gives the boundary traction $P_{\text{surf}}^{x=l_x}$ and $P_{\text{surf}}^{z=l_z}$ imposed on the face of $x = l_x$ and $z = l_z$ respectively. Eq. (28c) prescribes the displacement loading conditions along y-direction. The displacement evolution $U_y(t)$ along y-direction is transformed by

$$U_y(t) = l_y(t) \cdot \bar{\varepsilon}_{yy}(t) \tag{29}$$

It is emphasized that l_y evolves with time should be considered as larger elongation advances. $\bar{\varepsilon}_{yy}(t)$ is the average strain component over the volume of the target element. In addition, for the Al–Cu–Mg alloy studied, average grain size d is 14.7 μm using measurement techniques based on the number of grains intercepted per unit length of a test line. Grain boundary relative thickness is defined as $f_{\text{GBZ}} = 2t/d$ in which t and d are shown in Fig. 5(d). f_{GBZ} essentially represents the grain boundary volume fraction.

The boundary and loading conditions in this model differed from the traditional periodic boundary conditions in two ways. First, traditional periodic boundary conditions were used under the assumption of

macroscopic homogeneous deformation. The present conditions derived from the necking region were applied for the sake of description of stress state and continuity inside the sample, which conflicted with the assumption to some extent. Second, the above pressure loading conditions for the polycrystal aggregate as an RVE were not allowed to constitute a repeated sample.

In addition, two series of random distribution numbers from $-\pi$ to π are created and taken as the angle of crystal axis x' with respect to the global axis x and y. Similarly, crystal axis y' are chosen randomly in the plane perpendicular to axis x'. Crystal axis z' is determined so that x', y' and z' form a right-handed crystallographic basis. The randomly distributed orientations are checked through x–y plane pole figure to ensure the $\{1\,1\,1\}\langle 1\,1\,0\rangle$ slip system for each grain is uniformly distributed in the pole figure and no more than two points lie in the same position. Once the first slip system for a crystal lattice is determined, the other eleven slip systems can be obtained.

3.2. Mesh convergence and RVE size

3.2.1. Influence of the mesh size

To check the mesh convergence, several simulations are performed for the polycrystal aggregate including the same number of grains with different mesh sizes of 8-node brick elements. The region filled with grey color refers to the grain boundary layer in Fig. 6.

- Case 1 has 4 elements within each grain, and grain boundary layer consists of 2 elements or 1 element (Fig. 6(a)). There are a total of 1794 elements in the aggregate.
- Case 2 has 8 elements within each grain, and each grain boundary layer consists of 2 elements (Fig. 6(b)). There are a total of 2847 elements in the aggregate.
- In Case 3, there are 18 elements in each hexagonal grain. Each grain boundary layer consists of 3 elements (Fig. 6(c)). There are a total of 5149 elements in the aggregate.
- Case 4 has 32 elements in each hexagonal grain. Each grain boundary layer consists of 4 elements (Fig. 6(d)). There are totally 8138 elements in the aggregate.

A numerical comparison for four mesh sizes cases is performed as shown in Fig. 7. It is seen that the von Mises equivalent stress σ_{eq} and von Mises equivalent plastic strain ε_{eq}^{pl} over the volume are fairly similar for total 2847, 5149 and 8138 elements. However, the results by the total 1794 elements do not converge, in which the volume-averaged values of σ_{eq} is larger and ε_{eq}^{pl} is lower than the convergent one.

In order to investigate the effects of mesh size on shear bands, local plastic strain and stress based on GBM are examined. Fig. 8 shows the local equivalent plastic strain distribution when the remote tensile strain reaches 50%. These contours show that the deformation patterns are independent of the mesh size. The patterns become finer when the precision of the mesh increases. We now turn to consider the slip shearing behavior on all slip systems of grains inside one shearing band (denoted in Fig. 8). Variation of the accumulated slip strain for these grains is a measure of localized deformation that grains inside shear band develops to accommodate the total deformation. The results based on the four mesh size cases are

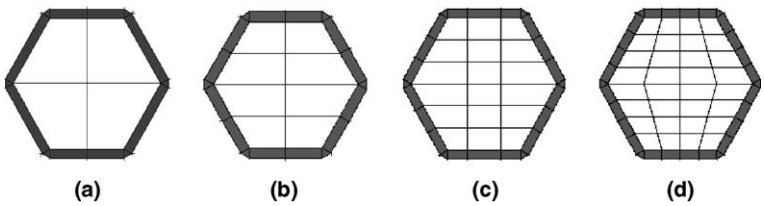

Fig. 6. Four mesh sizes for each hexagon grain and grain boundary layer.

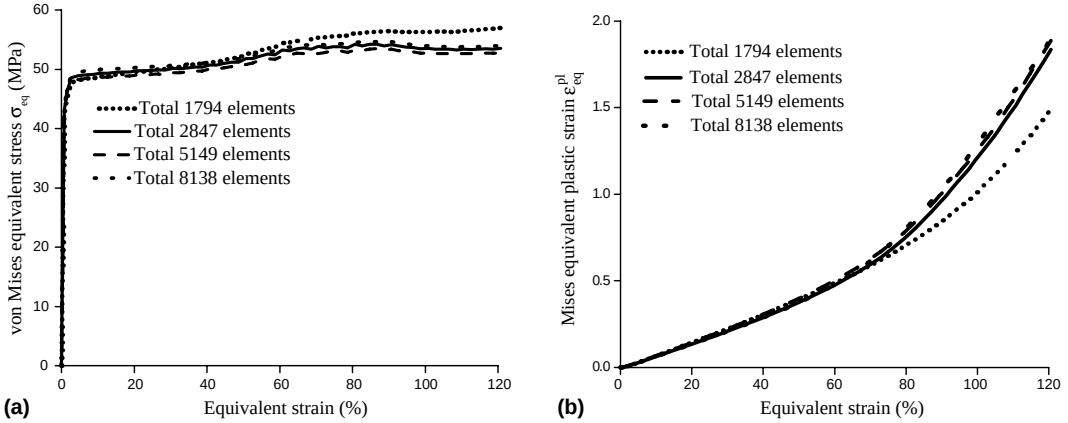

Fig. 7. Comparisons for the four mesh size cases with respect to (a) von Mises equivalent stress and (b) Mises equivalent plastic strain.

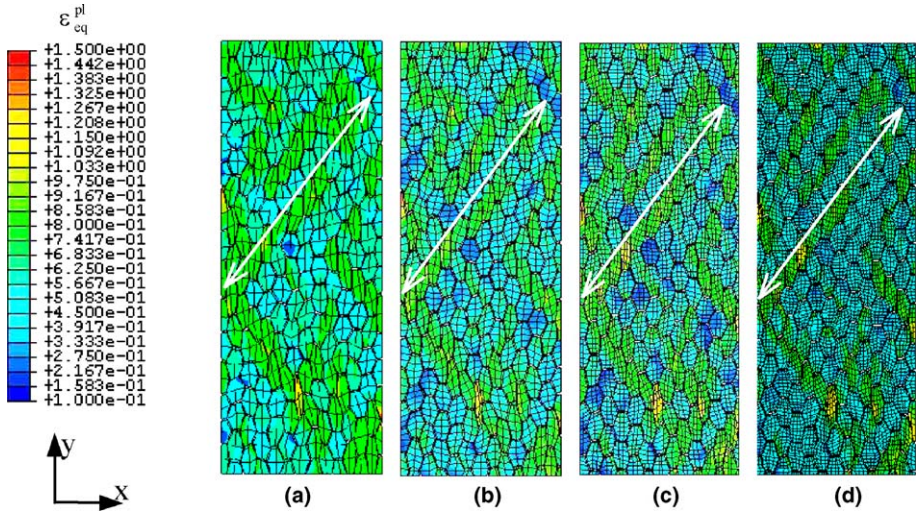

Fig. 8. Effect of the mesh size on the local behavior at 50% remote tension strain. (a) Case 1: 1794 elements; (b) case 2: 2847 elements; (c) case 3: 5149 elements; (d) case 4: 8138 elements.

compared in Fig. 9, from which we know that results by case 1 (total 1794 elements) also do not converge at that of the other three cases.

Furthermore, since the creation of shear bands and fracture initiation are heavily dependent on the local state of stress, we need to check the mesh convergence of local stress component distribution and their variations with time. We choose two paths and each includes ten points along x-direction, with which $y = 0.23l_y$, $z = 0.5l_z$ and $y = 0.5l_y$, $z = 0.5l_z$ respectively, as shown in Fig. 10(a). The corresponding values of stress components of all points along two paths are obtained using the same interpolation methods.

Curves reported in Fig. 10 show that discrepancy on local stress responses based on mesh size cases 2, 3, and 4 is very low. However, discrepancy on local stress components distributions by case 1 with only 4 elements per grain is significant. For a certain maximum error δ (e.g. 5%), if the mesh size cases make the relative errors between the magnitude of stress values are less than δ, we can say that such a mesh size is an

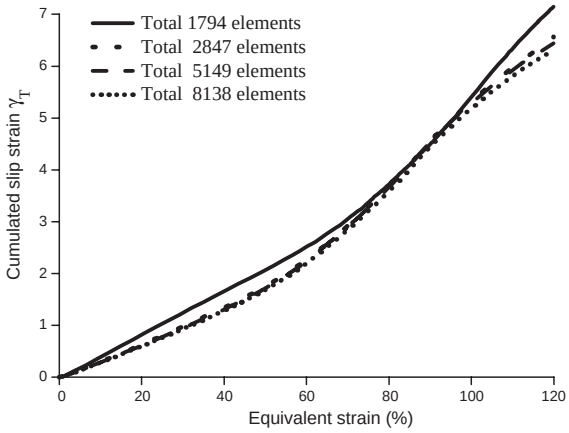

Fig. 9. Mesh size convergence analysis on variations of the accumulated slip strain γ_T with time within one shear band.

available mesh size. A relatively low number of elements (typically 2847) in which a volume contains 203 grains with 8 elements per grain can provide convergent description of the local stress field. It is known that evolution of damage variable is influenced by local stress, so we could also obtained the proper results of fracture and damage variable by total 2847 elements. In addition, mesh size inside grain boundaries seems not to be better with its size decreases through different mesh partition. Mesh size in grain boundaries should possess appropriate aspect ratio and fits the grain interior elements in size. About the dependence of fracture path on mesh sizes, we present the computed results in Section 4.4.3.

3.2.2. Representation of the RVE

The question of the minimum size of a RVE for a polycrystalline aggregate remains a central and unsolved question of the mechanics of heterogeneous materials. RVE size is material-property dependent so that the minimum RVE sizes for different properties are possibly different (Ren and Zheng, 2002). Drugan and Willis (1996) have ever performed an analytical work on the RVE size, using a non-local medium formulation. They employ a definition of an RVE as that of 'the smallest material volume element of the composite for which the usual spatially constant "overall modulus" macroscopic constitutive representation is a sufficiently accurate model to represent mean constitutive response. Their conclusion is that very small volumes, on the order of just a few grains, are required.

The microstructure of a polycrystal is mainly characterized by the sizes, shapes, and orientations of single crystal grains, the spatial distribution of grains, as well as the grain boundaries. The complexity of considering all the microstructural information is still overwhelming. The present simplified polycrystal model assumes that all grains included in a quasi-two-dimensional RVE are hexgona shape with the same grain size and randomly orientation distribution functions, so a RVE mostly depends on the number of grains along x- and y-axial directions as well as thickness.

A RVE should be large enough to smooth the local inhomogeneities and we take the different RVE sizes based on grain numbers n_x included along x-direction. The dimensions of RVE sizes along x-directions respectively are:

RVE-1 : $82.957 \times 107.546\ \mu m$; RVE-2 : $124.436 \times 155.478\ \mu m$; RVE-3 : $179.741 \times 218.789\ \mu m$
RVE-4 : $221.23 \times 267.32\ \mu m$; RVE-5 : $248.88 \times 298.68\ \mu m$; RVE-6 : $331.84 \times 394.54\ \mu m$
RVE-7 : $387.15 \times 458.45\ \mu m$

Length along y-direction is obtained by taking grain numbers along y-direction as $n_x + 1$.

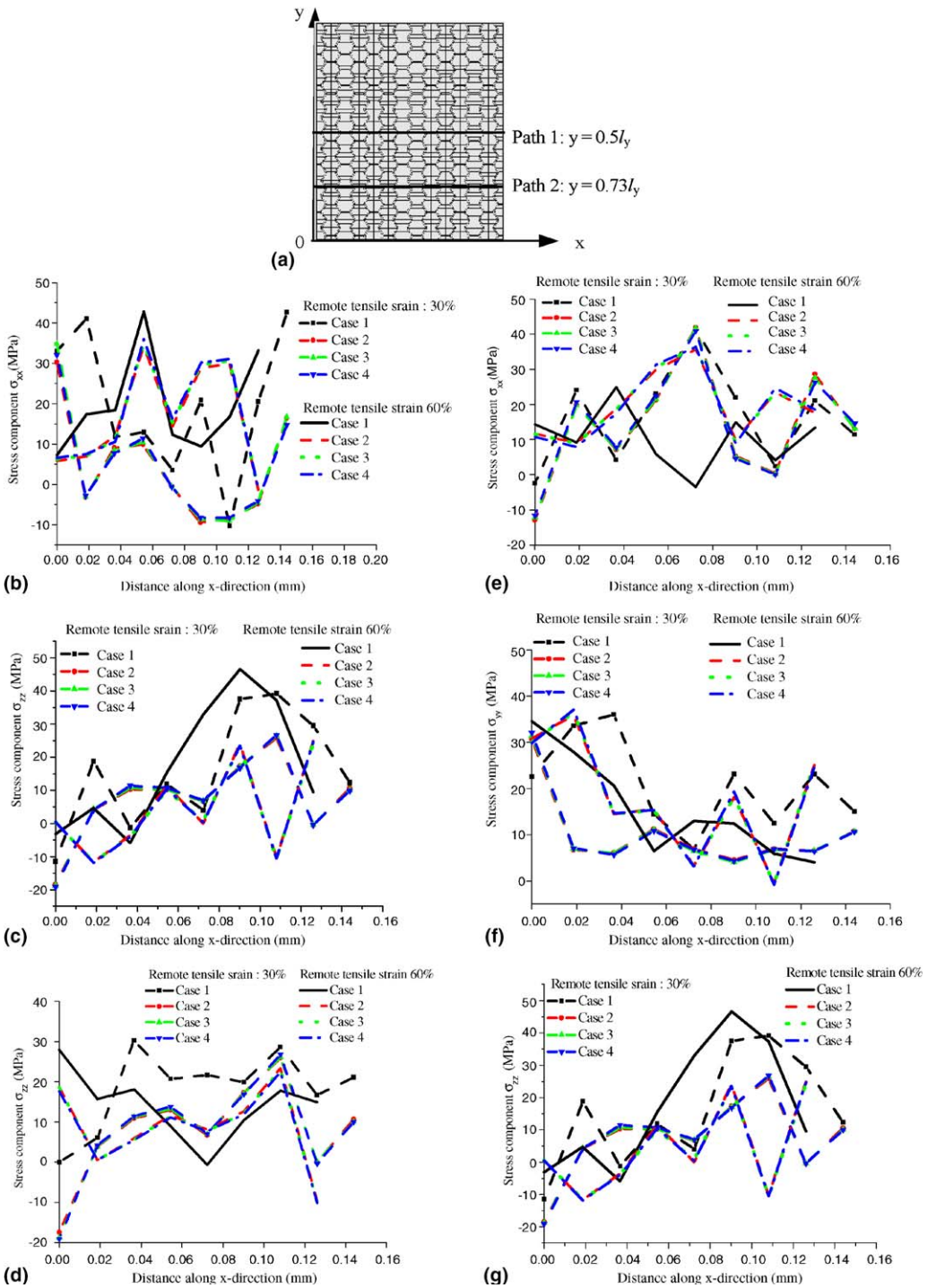

Fig. 10. Mesh size convergence on local stress component along two paths and their evolutions with remote tension strain increases: (a) two paths along x-direction; (b) σ_{xx}; (c) σ_{yy}; (d) σ_{zz} along path 1; (e) σ_{xx}; (f) σ_{yy}; (g) σ_{zz} along path 2.

By employing a scale-dependent boundary condition, volume-averaged value of stress/strain responses and yield points in the case of uniaxial tension are plotted in Fig. 11. Herein, yield points are chosen from Fig. 11(a) which corresponds to the equivalent strain of 1.5%. In general, more than one initial lattice orientations are assigned to construct the polycrystalline RVE for studying the homogeneous reactions. It is found that too little of the RVE size cause larger discrepancy with results by larger RVE size. The yield points in averaged stress–strain curves computed by the RVEs tend to reach the same stable value with the RVE size increases.

Furthermore, when grain boundary damage is taken into consideration, a number of numerical tests are carried out to demonstrate the ability of this model to describe the intergranular fracture behavior. The variation in grain boundary damage accumulation can be reflected by the decrease in the effective loading area. Fig. 12 shows the evolution of normalized effective area (A_e/A) versus tensile strain. A_e is expressed by

$$A_e = A - A_d \tag{30}$$

where A is the total transverse area and A_d is the transversal area by the eliminated elements at current time. $A_e/A = 1$ means that no damage has occurred in the aggregate and $A_e/A = 0$ means that a complete rupture has occurred. Fig. 12 shows the dependence of normalized effective area on RVE sizes, which could verify the RVE sizes from the damage and fracture aspect.

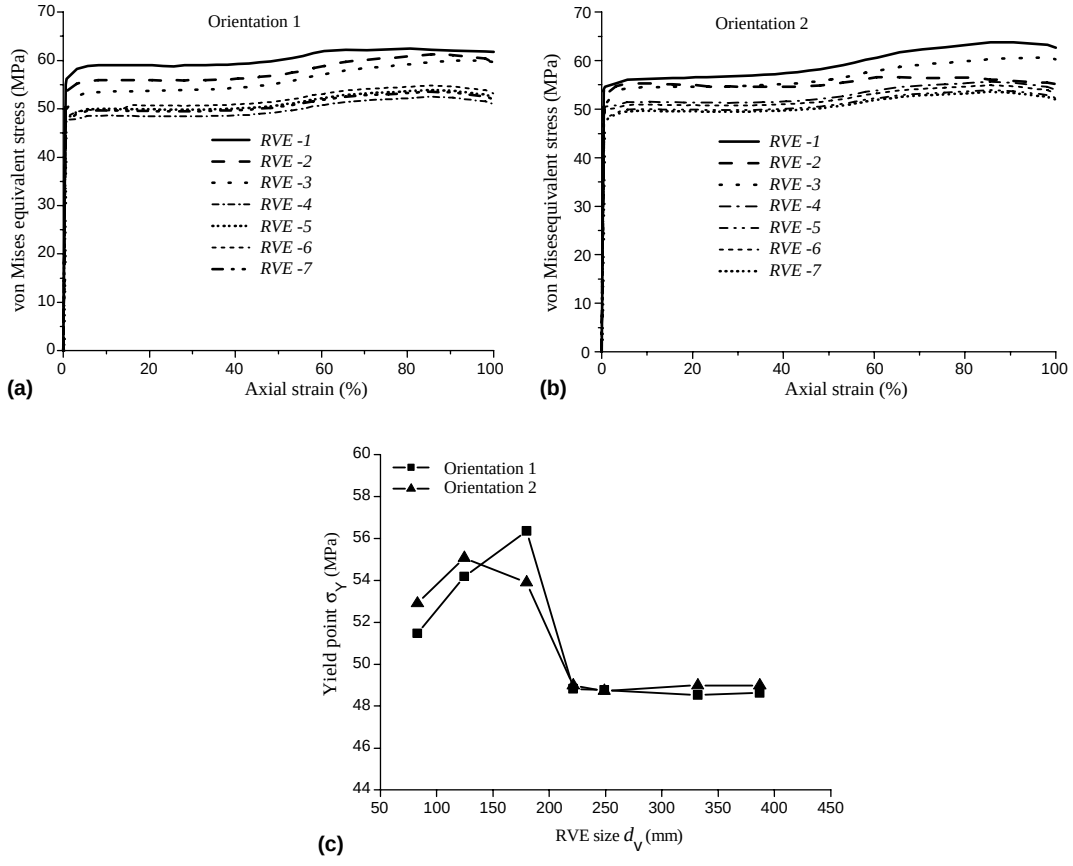

Fig. 11. (a) Volume-averaged von Mises stress/strain curves dependence on RVE sizes with regard to two different initial orientations and (b) dependence of yield point on RVE sizes.

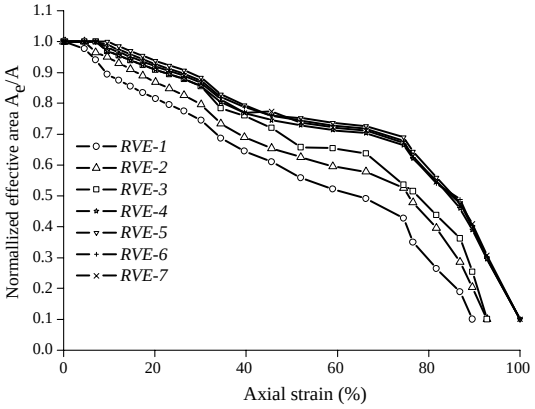

Fig. 12. Normalized effective area comparison for several RVE size when considering grain boundary damage.

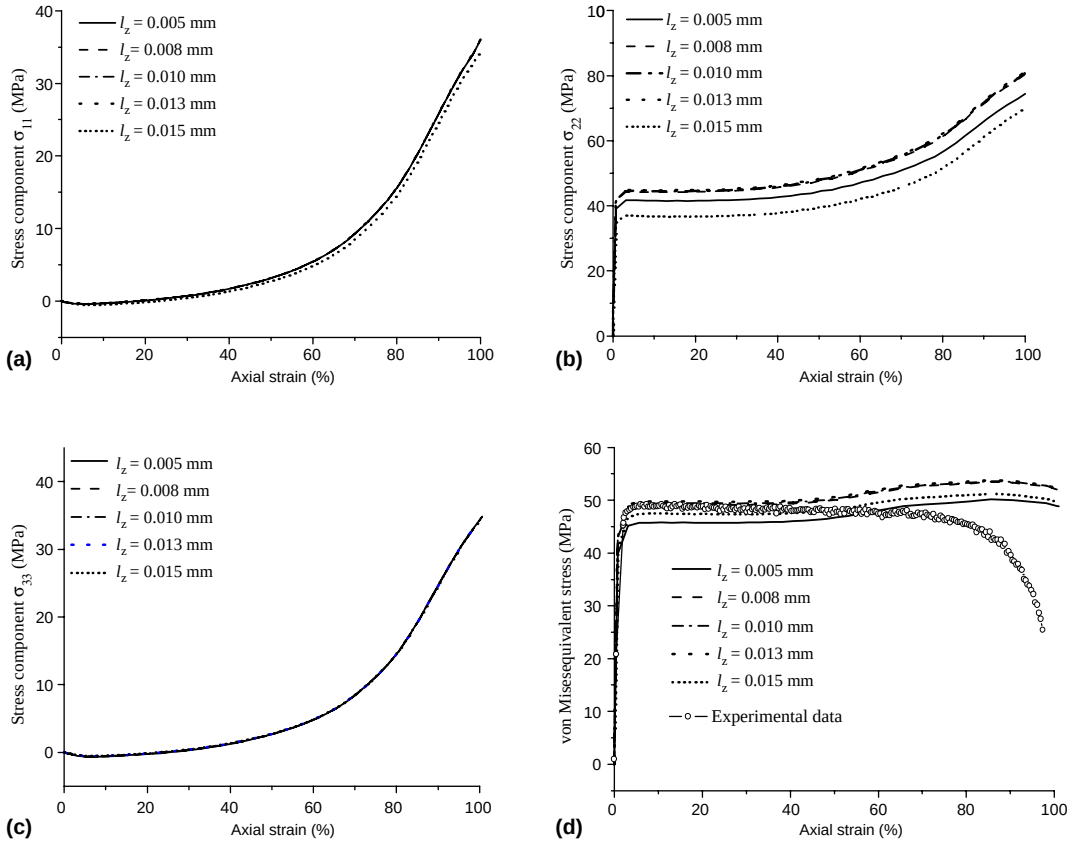

Fig. 13. Influence of quasi-2D RVE thickness on volume-averaged stress responses: (a) σ_{11}; (b) σ_{22}; (c) σ_{33}; (d) von Mises equivalent stress σ_{eq}.

It is demonstrated that the developed model gives successful results with dimension along y-axis is about 218.78 μm, which is 14 times grain size. Although the polycrystalline cube considered here is made of a smaller number grains but is not far from being a RVE at least for these loading conditions. So we select total 203 grains as the polycrystal model with y-direction dimension of 218.78 μm to investigate the effect of RVE thickness. Influence of RVEs thickness on the volume-averaged stress components and von Mises stress are shown in Fig. 13. It has been found that the stress components σ_{11}, σ_{33} are not very sensitive to the thickness of RVE. However, the stress component along the tensile direction (σ_{22}) is strongly dependent on thickness. Through comparisons between simulated von Mises equivalent stress and experimental results in Fig. 13(d), it is concluded that RVE with thickness of 0.08–0.013 mm could provide more accurate results.

According to the assumption of that the macroscopic response does not depend on the realization of the microstructure, the so called RVE has been developed based on the FEM technique. In the following, we take RVE size as $l_x \times l_y \times l_z = 179.741 \times 218.789 \times 10$ μm.

4. Results analysis

4.1. Effects of grain boundary relative thickness

Since the size scale is not included in constitutive equations of crystal plastic models. From the mechanics point of view, it is not the real physical thickness but is the size of influencing region. The grain boundary relative thickness changes with tensile strain rate and temperature have been discussed through experimental observations (Wu et al., 2002).

4.1.1. Stress state

The deformation and recovery of grain boundaries modifies the behavior in the zone close to it in many ways. One of the most important roles of grain boundary in polycrystal deformation lies in its influence on the local stress state. For high-temperature deformation, grain boundary void damage is considerably sensitive to stress triaxiality. As expected for a void growth mechanism of failure, the ductility decays exponentially with the stress triaxiality (Pardoen et al., 1998). The rupturing strain may be estimated through extrapolation (Pardoen et al., 2003).

Stress triaxiality is expressed as

$$R = \Sigma_{\mathrm{m}} / \Sigma_{\mathrm{eq}} \tag{31}$$

where $\Sigma_{\mathrm{m}} = \frac{1}{3}\Sigma_{kk}$ is the mean stress and $\Sigma_{\mathrm{eq}} = \sqrt{\frac{3}{2}\Sigma'_{ij}\Sigma'_{ij}}$ is the equivalent stress, Σ'_{ij} is the deviatoric stress.

Fig. 14 presents the influence of grain boundary relative thickness f_{GBZ} on the stress triaxiality of grain boundary and grain interior region respectively. As shown in Fig. 14(a), the volume-averaged stress triaxiality of grain boundaries increased with increased f_{GBZ}. In the case of $f_{\mathrm{GBZ}} = 0.14$ and $f_{\mathrm{GBZ}} = 0.20$, stress triaxiality in grain boundary zones remained constant when the remote strain was less than 70%. In the case of $f_{\mathrm{GBZ}} = 0.08$, stress triaxiality of the grain boundary first decreased and then increased abruptly when strain exceeded 70%.

In Fig. 14(b) shows that f_{GB} plays little role in the stress triaxiality of grain interiors calculated by GBM, while results obtained by NGBM show a much larger role than the former. Therefore it can be concluded that grain boundaries have the effect of reducing the stress triaxiality of grain interiors. However, grain boundary stress triaxiality increases with increased grain boundary relative thickness.

Note that the absolute value of stress triaxiality only represents a kind of stress state. The rupturing position in practice is also related to the probability of void nucleation. It is gradually recognized that triple junction structure and property may be completely different from the grain boundary in which it is located.

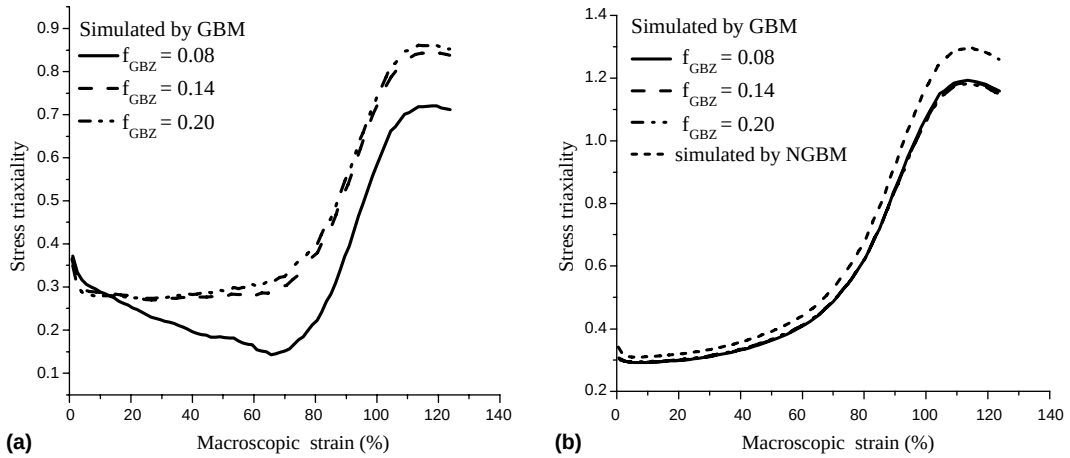

Fig. 14. Volume-averaged stress triaxiality of (a) grain boundary region and (b) grain interior region.

Elastic interactions between a grain's boundary and its neighboring grains is much stronger which makes the second phase particles tend to gather at triple junctions and then induce fracture.

4.1.2. Accumulated slip strain

The accumulated slip strain (γ) for all slip systems, which represents the deforming degree of grain interiors, is defined by the following expression:

$$\gamma = \sum_{\alpha} |\gamma^{(\alpha)}| \tag{32}$$

where α denotes the 12 slip system for FCC crystal.

The influence of f_{GBZ} on grain boundary effective plastic strain and grain interior accumulated slip strain is shown in Fig. 15.

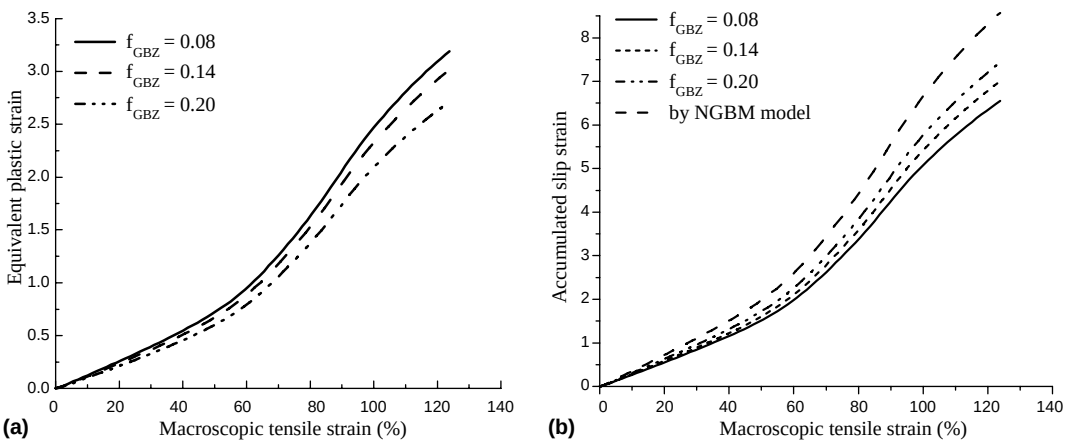

Fig. 15. Influence of f_{GBZ} on volume-averaged (a) effective plastic strain for grain boundary regions and (b) accumulated slip strain for grain interior regions.

With rising f_{GBZ}, the grain boundary equivalent plastic strain decreased and grain interior accumulated slip strain increased. This indicates that increasing the grain boundary relative thickness promotes grain interior slip deformation. For comparison purposes, simulated results using GBM and NGBM are also shown in Fig. 15(b). It is noted that the largest accumulated slip strain is obtained using NGBM, which indicates that grain interior anisotropic slip deformation is reduced when grain boundary is regarded as deformation carrier.

If the grain boundary indirectly reflects neighboring grain misorientation, which is described by NGBM, more grain interior slip strain is required to obtain the same global response than that calculated by GBM. In other words, the presence of grain boundary seems to suppress the grain interior slip deformation, while this suppressive role is reduced with increasing grain boundary relative thickness. It can be concluded that the role of the grain boundary is not a simple accumulative effects.

4.2. Grain rotations

Anisotropic slip deformation results in serious heterogeneous deformation and grain rotations at the microscopic scale. Experimental analysis of orientation rotation for the deformed polycrystals has been conducted at ambient temperature using focused hard X-ray (Margulies et al., 2001). It is now of interest to discover if (and if so, how) individual grain rotation is influenced by the presence of grain boundary layers at high temperatures.

During the static tensile deformation, to ensure that the two sides of any grain boundary are adjoined and in stress equilibrium at all times, the grains have to change their shapes in different ways and also their crystallographic orientations must rotate with respect to each other. Fig. 16 shows the inelastic equivalent strain contour for the polycrystal aggregate where the shear bands along some inclined directions were present. As the deformation proceeds, grains in shear bands became seriously elongated, while the shape of the grains in the non-shear bands changed little.

To investigate the influence of grain boundary on the behavior of an individual grain in detail, grains A and B inside the shear bands and grains C and D inside the non-shear bands were taken out from the deformed polycrystal model, as shown in Fig. 16. The maximum value of local inelastic strain by NGBM was

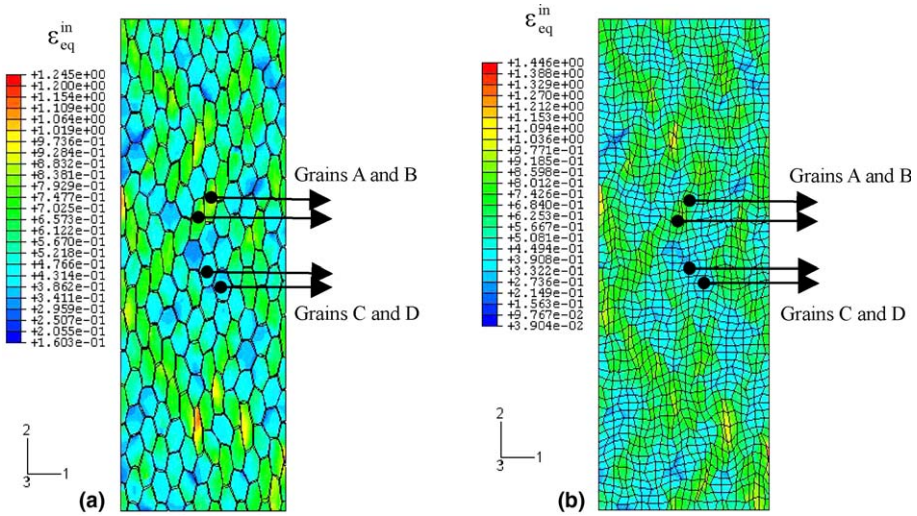

Fig. 16. Grains (A, B) in shear bands and (C, D) in non-shear bands taken out of (a) GBM and (b) NGBM.

higher than that of GBM. It was concluded that grain boundary has the effect of homogenizing the localized plastic deformation.

Volume-averaged local orientation to all integration points within the target grains was used to measure the lattice rotation of individual grains. The included angles between current and initial lattice orientation (e.g. [1 0 0], [0 1 0], [0 0 1]) were defined as α, β and ϕ (shown in Fig. 17(a)). The subscript '0' refers to the initial time and 't' refers to the current time.

On the other hand, mutual rotation in terms of two neighboring grains is also very important since many macroscopic effects result from grain interactions and interaccommodations especially if the grain boundary sliding is not neglected. To measure the mutual rotation of two neighboring grains quantitatively, one makes use of the angles ($\alpha(t)$, $\beta(t)$, $\phi(t)$) referring to the misorientation of the target neighboring grains [1 0 0], [0 1 0], [0 0 1] at time t (as shown in Fig. 18(b). The measurement of mutual rotation is defined as

$$\alpha_r = \alpha(t) - \alpha(0), \quad \beta_r = \beta(t) - \beta(0), \quad \phi_r = \phi(t) - \phi(0) \tag{33}$$

where $\alpha(0)$, $\beta(0)$, $\phi(0)$ are the misorientation of neighboring grains at $t = 0$.

The variation of angles α, β and ϕ of grain B with time is shown in Fig. 18. The value of α, β and ϕ obtained by GBM was higher than that calculated by NGBM for grain B inside shear bands. For grain C in non-shear bands, as shown in Fig. 19, α, β and ϕ decreased when taking grain boundary layer into account. Through analyses for multiple grains in shear and non-shear bands, the grain boundaries had the same effect on the individual grain rotation, i.e. the grain boundaries promoted the rotations of grains in shear bands and suppressed the rotation of grains in non-shear bands.

It was concluded that the increase in grain rotation inside shear bands leads to greater contribution of grain rotation to global deformation. Meanwhile, increasing the grain rotation may reduce the extent of localized plastic deformation. By contrast, grains in non-shear bands are those that do not have the obvious deforming tendency so they usually play the accommodation role during deformation. The decrease in grain rotation in non-shear bands indicated that the grain boundaries contribute more to global response.

Studies on mutual rotation of grains obtained further insights on grain boundary effects, as shown in Figs. 20 and 21.

Fig. 20 shows the mutual rotation (indicated by α_r, β_r, ϕ_r) of the A, B grain pair from GBM and NGBM. The results indicated that grain boundaries promote slight mutual rotation of two neighboring grains in shear bands. Similar comparison of grains C and D in non-shear bands was made as shown in Fig. 21. The results obtained that grain pair (C, D) in non-shear bands had a tendency that was similar to that

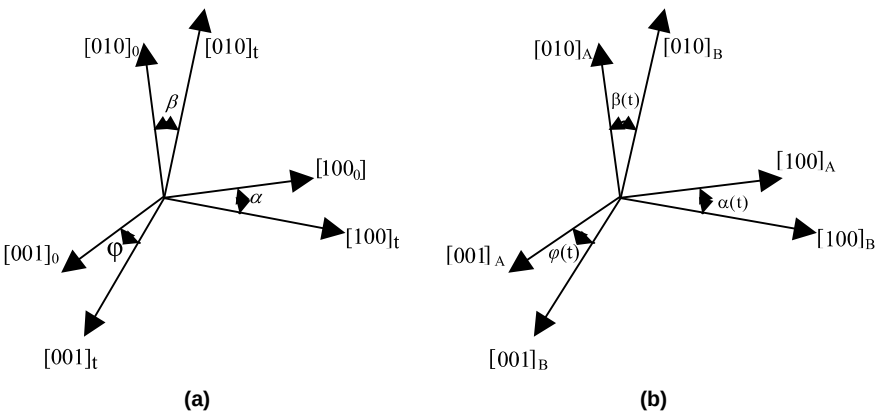

Fig. 17. Schematic representations for (a) measurement of individual grain rotation and (b) measurement of mutual rotation for two neighboring grains at time t.

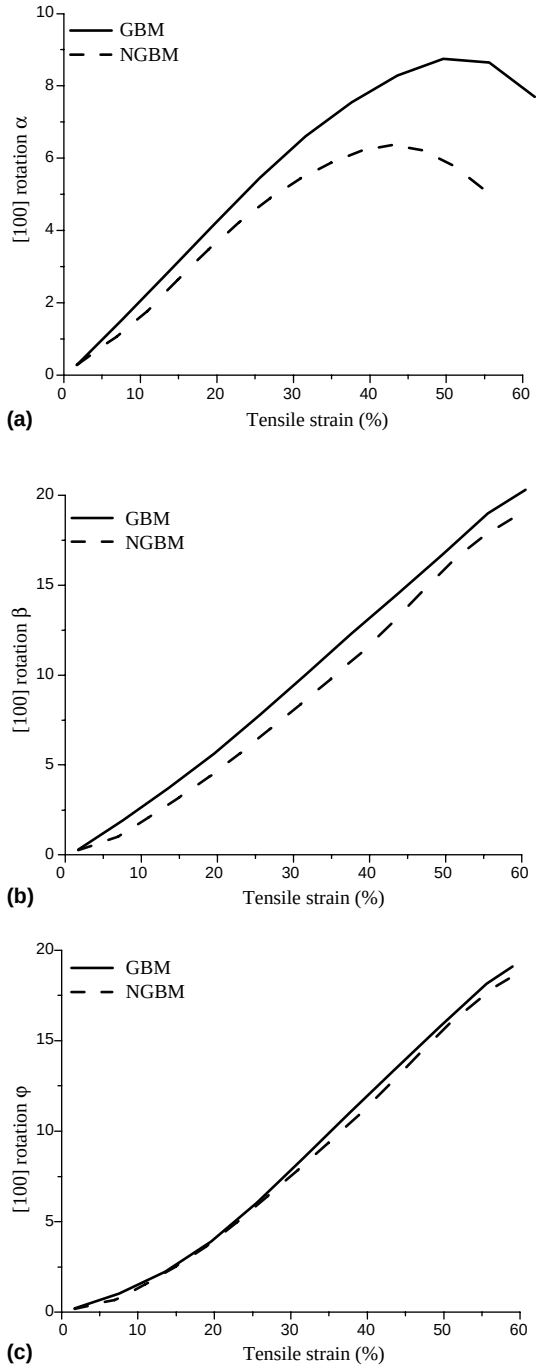

Fig. 18. Comparison between lattice rotation of grain B by GBM and that by NGBM in terms of crystal orientation: (a) [100]; (b) [010]; (c) [001].

of grain pair (A, B) in shear bands. It was found that grain mutual rotation both in and outside the shear bands were enhanced by the introduction of grain boundaries. In contrast to grain pair (A, B), the influence

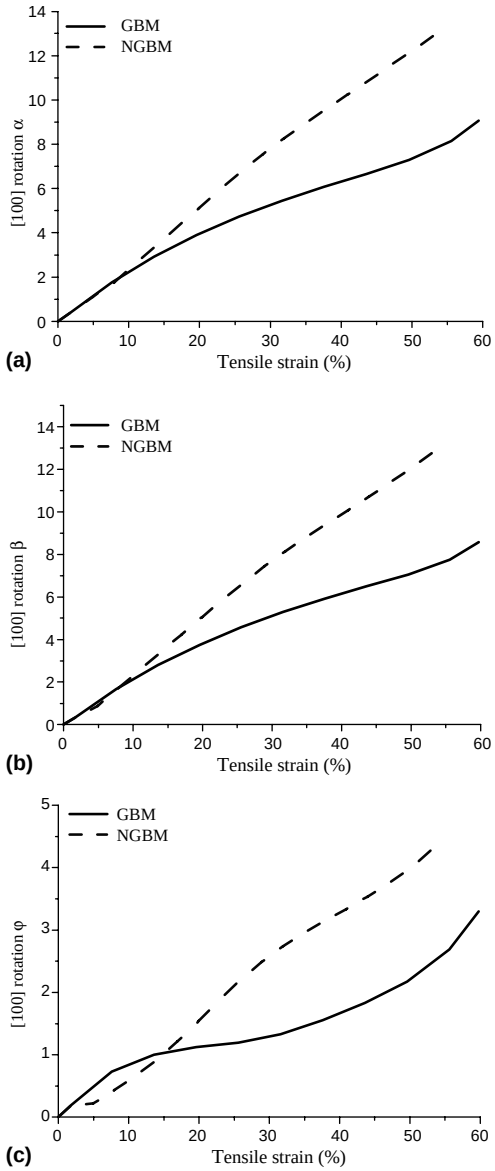

Fig. 19. Comparison between lattice rotation of grain C by GBM and that by NGBM in terms of crystal orientation: (a) [100]; (b) [010]; (c) [001].

of grain boundary on mutual rotation of grains C, D was more remarkable. This can be explained as the follows: grains in shear bands assume more plastic deformation while grains outside shear bands rotate strongly due to the contribution of grain boundaries.

4.3. Comparisons between experimental and simulated results

Grain boundary effects were further investigated through comparing experimental data reflecting rate-dependent characteristics with simulated results by GBM and NGBM. As shown in Fig. 22, the

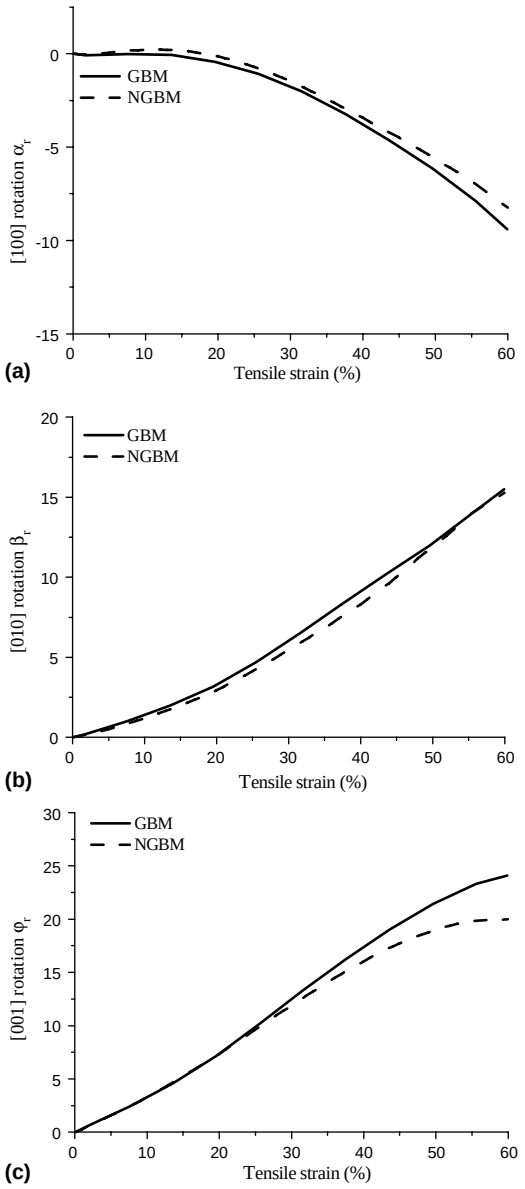

Fig. 20. Comparison between mutual rotations of grains A, B by GBM and NGBM in terms of crystal orientation: (a) [1 0 0]; (b) [0 1 0]; (c) [0 0 1].

volume-averaged tensile stress–strain curves based on GBM were in good agreement with experimental tensile curves at different strain rates. In contrast, NGBM could not determine the rate-dependent behavior of polycrystal at high temperatures. It was concluded that the rate-dependent characteristics under elevated temperatures strongly depend on the grain boundary microstructure and its viscous flow properties. Of course, more precise experimental work is required in the future for quantitative comparisons.

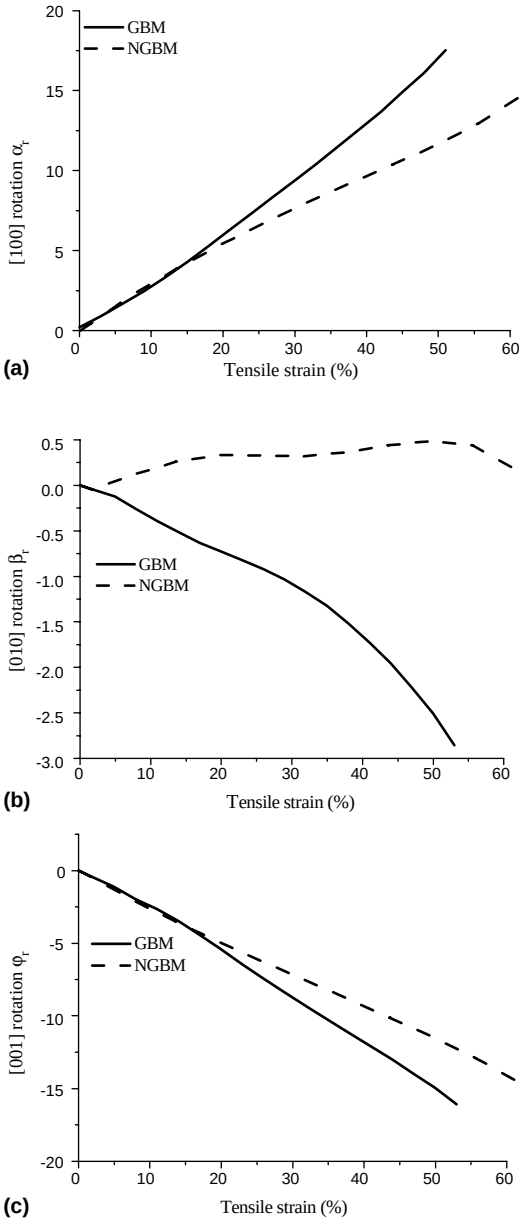

Fig. 21. Comparison between mutual rotations of grains C, D by GBM and NGBM in terms of crystal orientation: (a) [100]; (b) [010]; (c) [001].

At the same time, the microstructure of the material observed by transmission electronics microscopy (TEM) in the present study showed remarkable change in grain boundary region after stretching at 713 K and 753 K (shown in Fig. 23). The white strips indicate the participation of the grain boundary, which then left a trace accordingly. It was concluded that grain boundary acts more like an influencing region during high-temperature deformation.

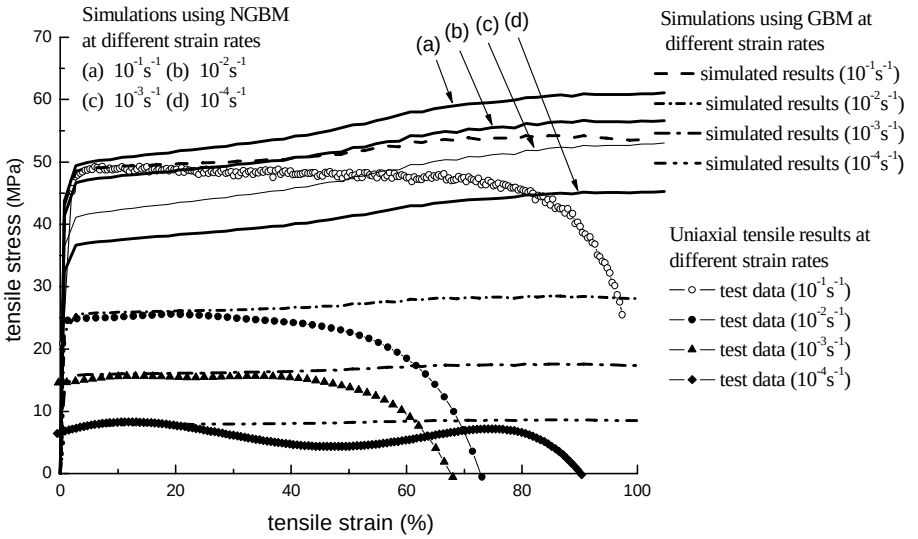

Fig. 22. Comparisons between test data and simulated results at different tensile rates using GBM and NGBM.

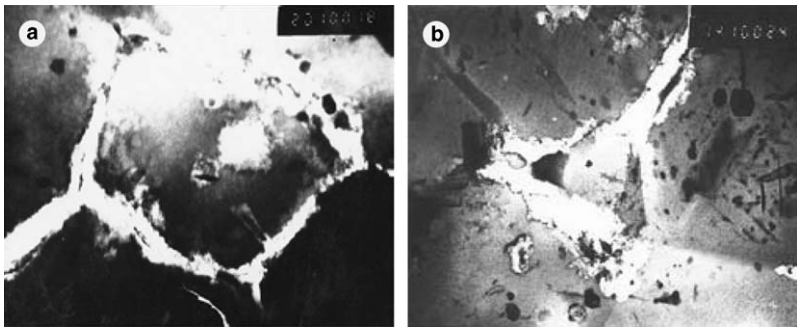

Fig. 23. Grain boundary characteristics after subjected to tension to fracture at (a) 713 K (20000×) and (b) 753 K (14000×).

4.4. Intergranular fracture

4.4.1. Uniaxial tensile simulations

Firstly, we consider a uniaxial tensile sample. As shown in Fig. 24, the predicted load–displacement curve using Chaboche viscoplastic damage model are in reasonable agreement with experimental data obtained at high temperature 753 K. For this material, after necking begins during a tensile test, it is still far from failure. The volume in the necking region experiences an increasing triaxiality of the stress state where plastic and damage characterizations are meaningful.

Thus, from the simulated macroscopic seriously necking region, one failure element is taken out from the deformed sample. The damage variable evolution Φ of this target element with time is shown in Fig. 25, from which it can be clearly seen that the critical value of the damage variable for this element may take $\Phi_{cr} = 0.73$. According to the concept of continuum damage, the damage variable Φ should fulfill $0 \leqslant |\Phi| \leqslant \Phi_{cr}$. $|\Phi| = 0$ and $|\Phi| = \Phi_{cr}$ correspond to the undamaged and completely failure state respectively.

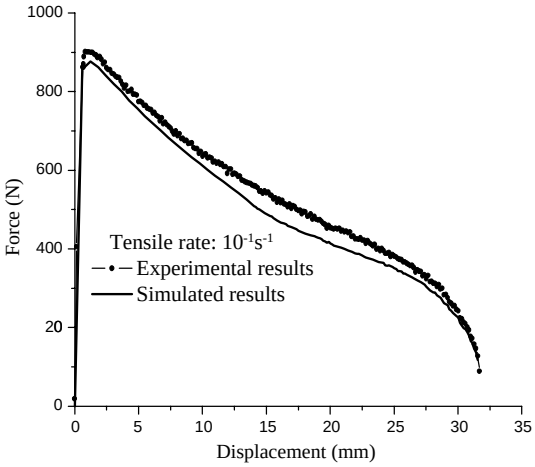

Fig. 24. The predicted results between numerical simulation and experimental data.

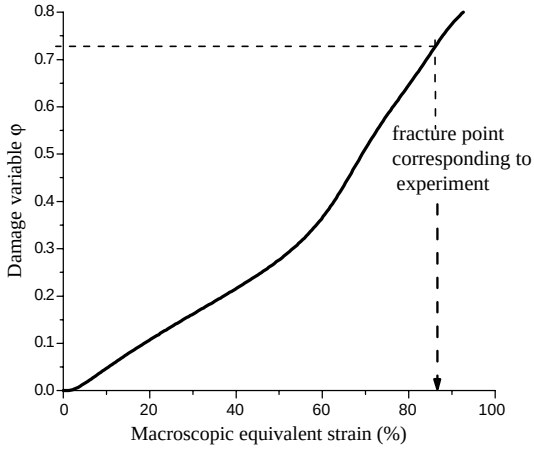

Fig. 25. Evolution of damage variable of the target failure element.

4.4.2. Global responses

The variation in grain boundary damage accumulation can be reflected by the decrease in the effective loading area. Similar to that of Fig. 12, the curve in Fig. 26 presents the evolution of normalized effective area (A_e/A) versus tensile strain. It is found that four stages are included in the whole process. Almost no failure element appears at the range of $\bar{\varepsilon} \leqslant 8\%$. Subsequently, at the range of $8\% < \bar{\varepsilon} \leqslant 33$, there is a linear relationship between the effective areas with macroscopic strain. As tension proceeds, the curve becomes gently inclined at the range of $33 < \bar{\varepsilon} \leqslant 71$, which reflects the gradually development of a fracture. The effective loading area is decreased abruptly when $\bar{\varepsilon} \geqslant 71\%$, which corresponded to a transition from a steady flow to an unstable deformation stage, and then the final fracture occurred quickly. After completely rupturing, it is found that about 40% failed elements fracture at the final stage and the effective load-carrying area decreased from 65% to 5% in this stage.

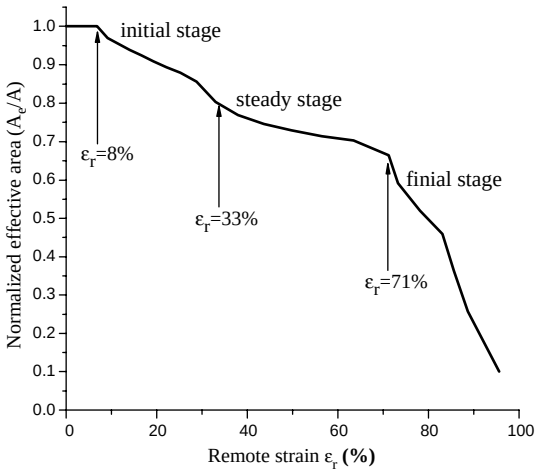

Fig. 26. Evolution of the normalized effective loading area during high-temperature deformation.

Another feature of this numerical model is that it can show the influence of the damage produced by grain boundaries on the mechanical response. Fig. 27 presents a comparison between the simulated stress–strain curves and the experimental results. The stress–strain curve simulated by GBM (the model not considering grain boundary damage) showed an obvious hardening when the axial strain was greater than 60%. However, the stress–strain curve calculated by DGBM (the model considering damage produced by grain boundaries and elements are removed when complete failure occurs) showed softening effects especially when a considerably large deformation was reached. The experimental results are in better agreement with the simulated results by DGBM. The reduction in flow stress, especially at the final stage, captured by the DGBM model may be ascribed to grain boundary damage and rupture. Note that intergranular failure elements do not significantly influence the global responses at the early deformation stage. In addition, the results from the GBM simulation coincided with the DGBM results when the deformation was lower than 50% or so.

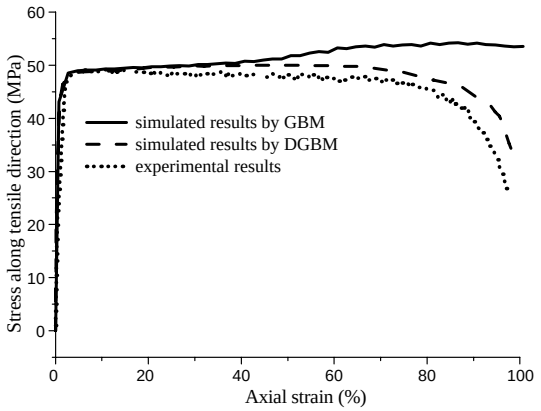

Fig. 27. Comparison of macroscopic experimental results with simulated results by the DGBM and GBM models.

4.4.3. Intergranular fracture path

One important aspect is the predicted evolution of the intergranular fracture path formed by completely ruptured grain boundary elements (shown in Fig. 28). The creation of the intergranular fracture path is

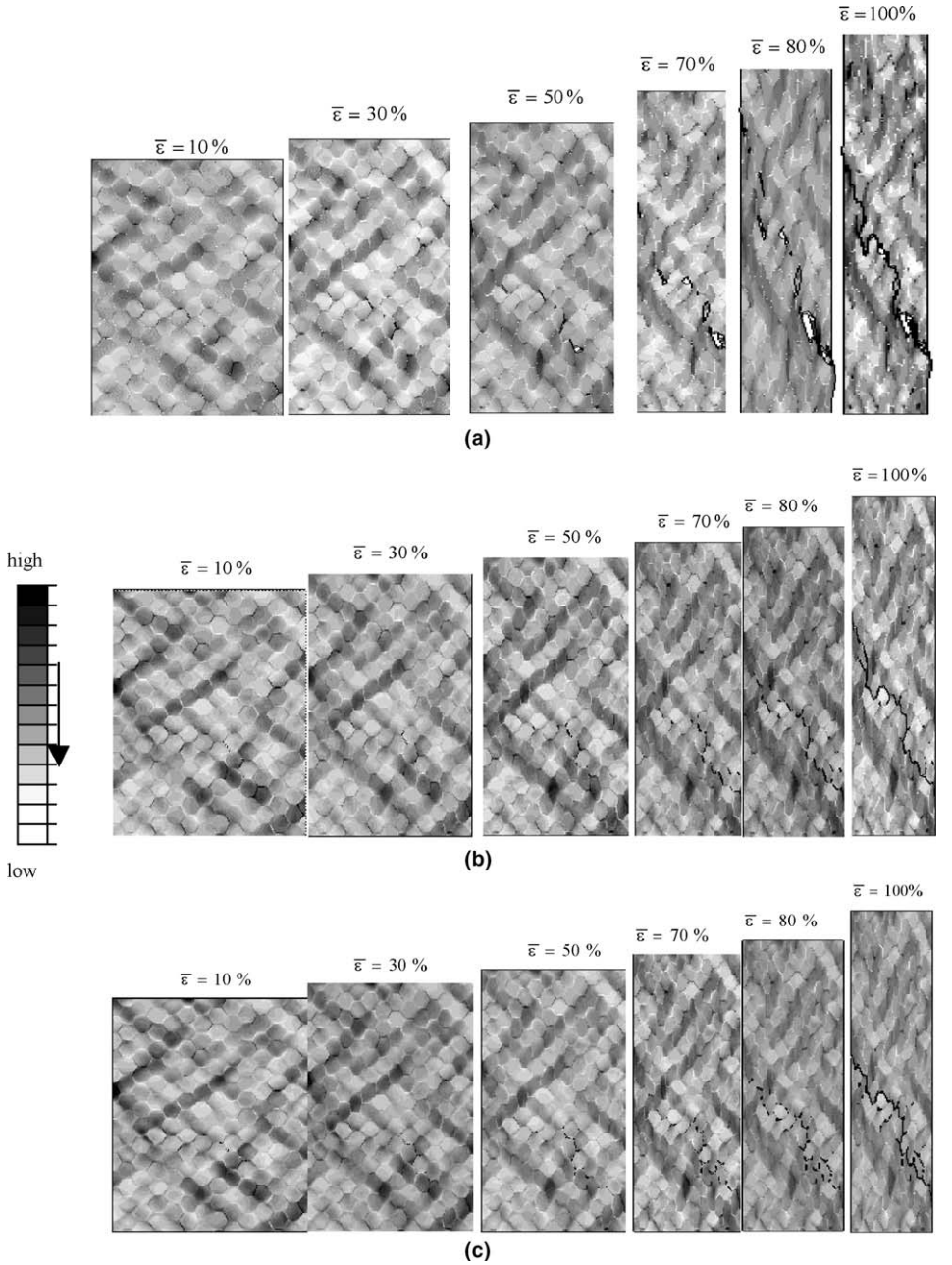

Fig. 28. Intergranular fracture path evolutions with remote tensile strains $\bar{\varepsilon}$ shown in the equivalent strain contour for different mesh size cases of (a) total 2847 elements, (b) total 5149 elements and (c) total 8138 elements. Different grey scale refers to the equivalent strain.

achieved by the failure and subsequent elimination of grain boundary elements. Thus, it is necessary to investigate the dependence of intergranular fracture path on mesh sizes. Fig. 28 simultaneity presents the fracture path evolution with remote tensile strain, in which different mesh size cases (2847 elements, 5149 elements, 8138 elements) could provide approximately similar intergranular fracture paths. It has been found that total 1794 elements with only four elements per grain case cannot give a convergent description of intergranular fracture path. According to these results, it is obvious that finer mesh case could give more details of the fracture process, where more failure elements dispersed around the fracture path than that in coarser mesh cases. Quite sharp fracture path and deformation structures appear in the coarser mesh.

The earliest ruptured element was a triple junction element located in the middle of the polycrystal aggregate shown at 10% tensile strain. Before the macroscopic equivalent strain reached 50%, the fractured elements are distributed dispersedly. Afterwards, these eliminated elements gradually form a continuous intergranular fractured path along the direction of bottom right to top left.

Even when grains are within a shear band, the motion, deformation and rearrangement of grains softens aggregates and creates additional geometric imperfections. However, from Fig. 28, the intergranular fracture path does not coincide with the most deformation. There is one point that should be clarified. Highly ductile materials are not so sensitive to crack or void. Much heterogeneity coexists and develops simultaneously, and their competition and interactions determine the final fracture. Determining which parameter should control damage accumulation is obviously a very important issue in the analysis of finite deformation. To the authors' knowledge, strain localization and stress concentration compete with each other at different locations that may determine the fracture mode in highly ductile materials. The accumulation of plastic shear strain will not necessarily determine the extent of grain boundary creep damage. This may be the reason that ductile fracture is so complicated.

4.4.4. Localized shear bands

The above simulated results indicate that the phenomenon of shear banding is triggered. Development of shear bands based on crystal plasticity has been widely investigated (Kuroda and Tvergaard, 2001). Studies on mesoscopic heterogeneity caused by local shear bands are very important in polycrystal deformation research (Watanabe et al., 1998; Makarov, 2000). In contrast to the previous interpretation, studies are focused on the influence of intergranular damage on the intensity of localized plastic strain which accounts for the organization of microstructures within a mesovolume.

In Fig. 29, the patterns of shear bands predicted by the GBM and DGBM have little difference, but the maximum equivalent plastic strain of the former is greater than that of the latter.

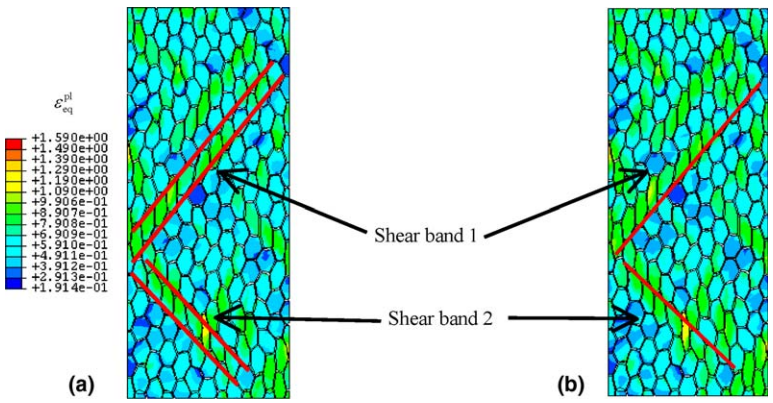

Fig. 29. Contour of equivalent plastic strain showing shear bands characteristics by the model (a) GBM and (b) DGBM at 50% macroscopic strain.

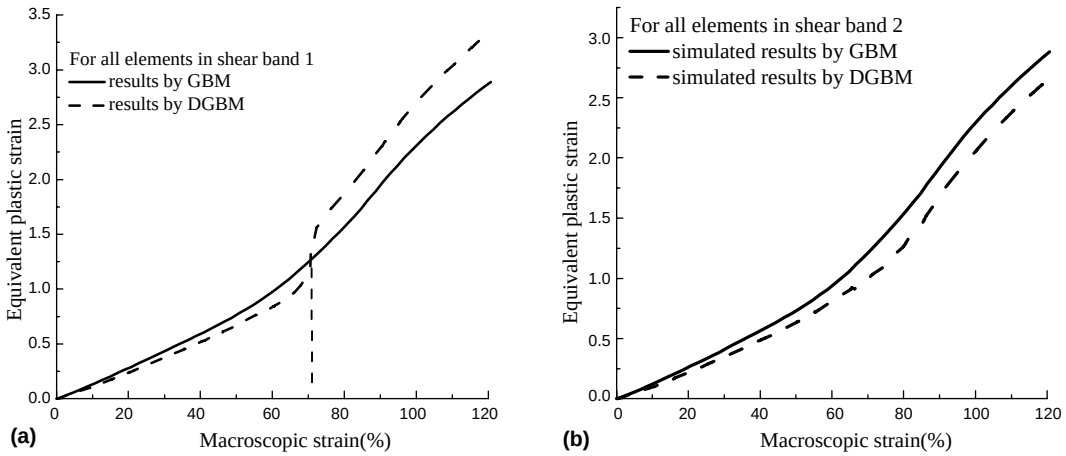

Fig. 30. Comparison of GBM and DGBM results for volume-averaged equivalent plastic strain for all grains in (a) shear band 1 and (b) shear band 2.

In order to quantify the effects of grain boundary damage, Fig. 30(a) and (b) provides a direct comparison between the variation of equivalent plastic strain in DGBM and GBM for all grains inside shear bands 1 and 2.

In Fig. 30(a), the difference between the two curves requires a detailed analysis. When the absolute equivalent strain was lower than 70%, the results calculated by DGBM were lower than that of GBM. Localized plastic deformation in shear band 1 could be reduced by removed fractured elements. It is known that most ruptured elements are located below shear band 1. Shear band 1 seemed to play a role of blocking the intergranular crack propagation. When $\varepsilon_{eq} > 70\%$, the predicted equivalent plastic strain by DGBM became larger than that of GBM. Combined with the observations of Fig. 26, Fig. 30(a) indicates the fact that a turning point of the curve simulated by DGBM corresponds to the unstable deformation. This might suggest that localized deformation in shear band 1 is accelerated by the intergranular damage at the final fracture stage.

Similarly, Fig. 30(b) shows the influence of grain boundary damage on shear band 2. As presented in Fig. 29, the deformed geometry of shear band 2 shows that it was almost parallel to the intergranular crack propagation path. In contrast to Fig. 30(a), the equivalent plastic strain of shear band 2 by DGBM is lower than that by GBM. The intergranular damage and fracture have reduced the local intensity of shear band 2. A comparison between the main feature of Fig. 30(a) and (b) indicates that shear band 1 could capture the global deformation characteristics more accurately than shear band 2.

5. Discussion

(1) Grain boundaries are intrinsic to the deformation of polycrystalline materials, both joining and separating the variously oriented component crystals. In the present study, two sets of simulations by GBM and NGBM described the net influence of grain boundary plasticity on the lattice rotation, slip deformation, and stress state. Despite the simplicity of the identical hexagon grains surrounded by grain boundary layers with certain thickness, the heterogeneous deformation characteristics were developed.

(2) Note that simulations predicted several shear bands intersecting the polycrystal aggregate. The analysis for many grains both in shear and non-shear bands showed similar effects of grain boundary on

the individual grain rotations. It was found that the grain boundaries promoted the rotation of grains in shear bands but suppressed the rotation of grains out of shear bands. This can be explained by the fact that the role played by the grain boundaries to shear band grains is different from to non-shear band grains. This led to the conclusion that an increase in the rotation angle is caused by grain boundaries viscous flow for high-temperature polycrystal deformation.

(3) Local grain interactions and grain boundary behaviors usually can be examined using samples made of either bicrystals and tricrystals or two-dimensional multicrystals. However, for polycrystals, due to the lack of experimental input, many models based on global assumptions could not take the different surroundings of individual grains into account. Tatschl and Kolednik (2003) have developed an experimental procedure to systematically investigate the local deformation behavior of polycrystalline materials at the micrometer scale. Their experiments showed that at some grain boundaries, very high lattice rotations can be observed. But they have omitted the data very close to the boundary and have not yet solved the problem of the data interpolation at the grain boundary. In the present study, the test flow curves were especially rate-dependent and this characteristic was captured by GBM, not by NGBM. Therefore, the influence of strain rate on polycrystalline materials behavior may be ascribed to the accommodation deformation by the grain boundary viscous flow during elevated-temperature deformation. This prediction provides some fundamental understanding about grain boundary effects on polycrystal plasticity. Grain boundary behavior may be regarded as a pointer to the property of rate-dependent plastic deformation. Furthermore, the reduction in flow stress at the final stage can be captured by the DGBM model which can be ascribed to grain boundary damage and rupture.

(4) When considering damage produced by grain boundaries (DGBM), both the effective loading area evolution and global responses could represent the characteristics of practical fracture processes to some extent. The most interesting result is a dramatic turning point in the curves of Fig. 30, which indicates that the localized deformation of shear band 1 was more susceptible to grain boundary damage than shear band 2. This finding implies strong interactions between various heterogeneities within ductile materials. Note that by considering the grain boundary, the model is capable of capturing these characteristics.

6. Concluding remarks

In this study, the grain boundary was regarded as an influencing zone in the 3D polycrystal aggregate model. This paper presented a series of grain boundary effects on local and global responses during high-temperature plastic deformation. To evaluate the role of the grain boundary at the mesoscopic level, a comparison between results from GBM and NGBM is very effective. From a micromechanics point of view, grain boundaries have the effect of promoting lattice rotation of individual grains within shear bands while suppressing that of grains outside shear bands. In the uniaxial tension cases, the predicted rate-dependent properties obtained based on the GBM model are in better agreement with experimental observations at high temperature than that on NGBM. These numerical simulations have shown that the deformation is sensitive to the presence of grain boundary regions. At the same time, an unstable flow at the final stage can be captured by DGBM but not by GBM, indicating that the DGBM model is more appropriate for describing the relationship between high-temperature fracture characteristics and the corresponding mesoscopic structural changes.

Acknowledgements

Y.-Q. Wu would like to express her gratitude to the two reviewers for their many constructive comments that led to substantial revisions. The financial support provided by the Chinese National Natural Science

Foundation No. 50371042 and 10276020, the Special Funds for the Major State Basic Research Projects 2004CB619304, the Key Grant Project of Chinese Ministry of Education No. 0306, and the financial support of the Postdoctoral Science Foundation of China under Grant No. 20040350031 are acknowledged.

References

Bower, A.F., Wininger, E., 2004. A two-dimensional finite element method for simulating the constitutive response and microstructure of polycrystals during high temperature plastic deformation. J. Mech. Phys. Solids 52, 1289–1317.

Cao, W.D., Lu, X.P., Conrad, H., 1996. Whisker formation and the mechanism of superplastic deformation. Acta Mater. 44, 697–706.

Drugan, W.J., Willis, J.R., 1996. A micromechanics-based nonlocal constitutive equation and estimates of representative volume element size for elastic composites. J. Mech. Phys. Solids 44, 497–524.

Fleck, R.G., Taplin, D.M.R., Beevers, J., 1975. An investigation of the nucleation of creep cavitaties by MV electron microscopy. Acta Metall. 23, 415–424.

Gifkins, R.C., 1994. Grain-boundary participation in high-temperature deformation: an historical review. Mater. Charact. 32 (2), 59–77.

Hanson, D., Wheeler, W.A., 1931. The deformation of metals and prolonged loading, the flow and fracture of Al. J. Inst. Metals 55, 229–257.

Hasegawa, T., Yasuno, T., Nagai, T., Takahashi, T., 1998. Origin of superplastic elongation in aluminum alloys produced by mechanical milling. Acta Mater. 46 (17), 6001–6007.

Hermann, R., 1987. Fracture at High Temperatures. Springer-Verlag, Berlin, Heidelberg.

Hutchinson, J.W., 1976. Bounds and self-consistent estimates for creep of polycrystalline materials. Proc. R. Soc. Lond. A 348, 101–127.

Kim, H.K., Lavernia, E.J., Earthman, J.C., 1992. Mechanisms of intergranular cavity growth in Ni3Al (Zr,B). Acta Metall. Mater. 40 (8), 1933–1943.

Koike, J., Mabuchi, M., Higashi, K., 1995. In situ observation of partial melting in superplastic aluminum alloy composites at high temperatures. Acta Metall. Mater. 43, 199–206.

Kuroda, M., Tvergaard, V., 2001. Shear band development predicted by a non-normality theory of plasticity and comparison to crystal plasticity predictions 38 (50–51), 8945–8960.

Langdon, T.G., 1993. The role of grain boundaries in high temperature deformation. Mater. Sci. Eng. A 166 (1-2), 67–79.

Lee, S., Utsunomiya, A., Akamatsu, H., et al., 2002. Influence of scandium and zirconium on grain stability and superplastic ductilities in ultrafine-grained Al–Mg alloys. Acta Mater. 50, 553–564.

Lemaitre, J., Chaboche, J.-L., 1990. Mechanics of Solid Materials. Cambridge University Press, Cambridge, New York.

Makarov, P.V., 2000. Localized deformation and fracture of polycrystals at mesolevel. Theor. Appl. Fracture Mech. 33 (1), 23–30.

Margulies, L., Winther, G., Poulsen, H.F., 2001. In situ measurement of grain rotation during deformation of polycrystals. Science 291, 2392–2394.

Mecking, 1981. In: Hansen, N., Horsewell, A., Leffers, T., et al. (Eds.), Deformation of Polycrystals: Mechanisms and Microstructures. Riso Natl. Lab., Denmark, pp. 73–86.

Meissonnier, F.T., Busso, E.P., O'Dowd, N.P., 2001. Finite element implementation of a generalized non-local rate-dependent crystallographic formulation for finite strains. Int. J. Plast. 17, 601–640.

Meyers, M.A., Benson, D.J., Vöhringer, O., Kad, B.K., Xue, Q., Fu, H.H., 2002. Constitutive description of dynamic deformation: physically-based mechanisms. Mater. Sci. Eng. A 322, 194–216.

Nakamachi, E., Hiraiwa, K., Morimoto, H., Harimoto, M., 2000. Elastic/crystalline viscoplastic finite element analyses of single- and poly-crystal sheet deformations and their experimental verification. Int. J. Plast. 16, 1419–1441.

Pardoen, T., Doghri, I., Delannay, F., 1998. Experimental and numerical comparison of void growth models and void coalescence criteria for the prediction of ductile fracture in copper bars. Acta Mater. 46 (2), 541–552.

Pardoen, T., Dumont, D., Deschamps, A., et al., 2003. Grain boundary versus transgranular ductile failure. J. Mech. Phys. Solids 51 (4), 637–665.

Rabotnov, Yu.N., 1969. Creep Problems of Structural Members. North-Holland, Amsterdam.

Raj, R., Ashby, M.F., 1975. Intergranular fracture at elevated temperature. Acta Metall. 23, 653–666.

Ren, Z.-Y., Zheng, Q.-S., 2002. A quantitative study of minimum sizes of representative volume elements of cubic polycrystals: numerical experiments. J. Mech. Phys. Solids 50, 881–893.

Shen, Y.L., Li, W., Sulsky, D.L., et al., 2000. Localization of plastic deformation along grain boundaries in a hardening material. Int. J. Mech. Sci. 42, 2167–2189.

Takayama, Y., Tozawa, T., Kato, H., 1999. Superplasticity and thickness of liquid phase in the vicinity of solidus temperature in a 7475 aluminum alloy. Acta Mater. 47 (4), 1263–1270.

Tatschl, A., Kolednik, O., 2003. On the experimental characterization of crystal plasticity in polycrystals. Mater. Sci. Eng. A 356, 447–463.

Tvergaard, V., 2004. Prediction of mixed mode interface crack growth using a cohesive zone model for ductile fracture. J. Mech. Phys. Solids 52, 925–940.

Watanabe, O., Zbib, H.M., Takenouchi, E., 1998. Crystal plasticity: micro-shear banding in polycrystals using Voronoi tessellation. Int. J. Plast. 14 (8), 771–788.

Wu ,Y.Q., 2003. Mesoscopic mechanical behavior of polycrystalline materials subjected to large deformation at elevated temperature. Doctoral dissertation. Northwestern Polytechnical University (in Chinese).

Wu, Y.Q., Zhang, K.S., et al., 2002. Coarse-grained superplastic deformation mechanisms of LY-12. Chin. J. Nonferrous Metals 12 (5), 986–990 (in Chinese).

Yoshida, H., Yokoyama, K., Shibata, N., et al., 2004. High-temperature grain boundary sliding behavior and grain boundary energy in cubic zirconia bicrystals. Acta Mater. 52 (8), 2349–2357.

Zavattieri, P.D., Espinosa, H.D., 2001. Grain level analysis of crack initiation and propagation in brittle materials. Acta Mater. 49, 4291–4311.

Zavattieri, P.D., Raghuram, P.V., Espinosa, H.D., 2001. A computational model of ceramic microstructures subjected to multi-axial dynamic loading. J. Mech. Phys. Solids 49, 27–68.

Zhang, K.S., Wu, M.S., Feng, R., 2005. Simulation of microplasticity-induced deformation in uniaxially strained ceramics by 3-D Voronoi polycrystal modeling. Int. J. Plast. 21, 801–834.